

MANUPULATING THE MAGNETIC DOMAINS OF HOLE-DOPED MANGANITES BY
USING ELECTRIC FIELD

By

TARA P. DHAKAL

A DISSERTATION PRESENTED TO THE GRADUATE SCHOOL
OF THE UNIVERSITY OF FLORIDA IN PARTIAL FULFILLMENT
OF THE REQUIREMENTS FOR THE DEGREE OF
DOCTOR OF PHILOSOPHY

UNIVERSITY OF FLORIDA

2008

© 2008 Tara P. Dhakal

To my parents

ACKNOWLEDGMENTS

My graduate studies at the University of Florida have been a great learning experience because of so many people and facilities available at the university. First and foremost I would like to thank my advisor Prof. Amlan Biswas for providing me a stress free environment to do research and studies. His willingness to help me and my lab mates at any time at any level is very much appreciated. The fact that he was a new faculty member gave me exposure to a lot of new things like setting up cryogenics, writing data acquisition programs, designing, etc.

I had the opportunity to take graduate level courses from very experienced teachers of our physics department for which I will always be thankful. I also would like to thank my supervisory committee members Prof. Arthur Hebard, Prof. Yoonseok Lee, Prof. Dmitri Maslov and Prof. Cammy Abernathy for providing valuable suggestions and guidance during my qualifying exam presentation and other times. In particular I would like to thank Prof. Hebard for providing me an opportunity to collaborate in projects like magneto-capacitance of capacitance structures in which manganites were used as one of the electrodes. I also would like to thank Prof. David Tanner for a collaborative opportunity to do optical measurements on some of the manganites.

I would like to thank my lab mates for their friendship, company and encouragement. I have to thank Sung Hee for her readiness to discuss physics problems with enthusiasm and deep insight. I would like to thank Jacob and Devesh for helping me with anything including film growth and designing. I have so many friends to be thankful for. I would like to thank Sinan, Naveen, Guneeta, Sef, Rajiv, Ritesh, Pradeep, Jun, Abhijit, Priyank, Emre, Cem, Susumu and all the others for being my very good friends and also helping me to broaden my research experience. I also would like to thank everybody in machine shop and in nanofabrication lab for making them such a convenient place to get things done quickly. I also would like to thank

people in cryogenics for providing liquid helium and liquid nitrogen 24/7. I would also like to thank Bob for making lab teaching a fun experience like providing pizza with nominal price during practice sessions. I would like to thank the janitors who keep the department neat, clean and hygienic for all of us.

My parents have been a source of inspiration for me. I would not be able to come to this point without their selfless sacrifice. I would like to thank them for providing me care and love and everything possible. I am also grateful to my wife Kasumi who has tirelessly taken care of my two beautiful daughters while providing me free time to come to school. And finally I would like to thank Mira and Kara for their precious smiles which would always cheer me up.

TABLE OF CONTENTS

	<u>page</u>
ACKNOWLEDGMENTS	4
LIST OF TABLES	8
LIST OF FIGURES	9
ABSTRACT	11
CHAPTER	
1 INTRODUCTION	13
Double Exchange Mechanism	13
Crystal Structure of the Manganites	14
Colossal Magnetoresistance, I-M Transition and Magnetism	15
Jahn Teller Distortion	18
2 PHASE COEXISTANCE IN MANGANITES: PR SUBSTITUTION.....	25
3 MATERIALS AND EXPERIMENTAL METHODS.....	33
Pulsed Laser Deposition	33
Atomic Force Microscopy	34
Transport Measurements	36
Magnetization Measurements	36
4 ELECTRIC FIELD EFFECT	47
Motivation.....	47
Experimental Details	49
Results and Observations.....	50
Hysteresis in Resistivity	50
Phase Diagram.....	50
Nature of Phase Coexistence	51
Nonlinear Current to Voltage Characteristics	53
Conclusion.....	55
5 ANISOTROPY IN TRANSPORT PROPERTIES OF MANGANITES	61
Motivation.....	61
Experimental Results and Discussion.....	62
Magnetization as a Function of Electric Field.....	62
Nanofabrication of a Cross Structure	64
Transverse Resistance by Lock-in Amplifier	65

Conclusion.....	66
6 SCANNING TUNNELING MICROSCOPY.....	74
Motivation.....	74
Basic Principle of Scanning tunneling Microscopy.....	74
Topography of Sample Surface	75
STM Spectroscopy.....	75
Designing Low Temperature Scanning Tunneling Microscope.....	76
Approach Mechanism.....	77
Current to Voltage Converter	78
Feedback System	78
Summing Circuit.....	79
Imaging Graphite.....	80
Scanning Tunneling Potentiometry	81
7 CONCLUSION AND FUTURE WORK.....	95
Conclusion.....	95
Future Work.....	95
Scanning Tunneling Potentiometry	95
Multiferroics.....	96
LIST OF REFERENCES.....	97
BIOGRAPHICAL SKETCH	102

LIST OF TABLES

<u>Table</u>		<u>page</u>
1-1	Ionic radii of different ions in LPCMO manganite.....	20
3-1	Lattice mismatch strain of the film LPCMO grown on different substrates.....	38

LIST OF FIGURES

<u>Figure</u>	<u>page</u>
1-1 Double exchange of e_g electron in two Mn sites via oxygen $2p$ state.....	21
1-2 Structure of the manganites with perovskite lattice.....	22
1-3 Reduction of resistivity by a magnetic field as a function of temperature in the compound $\text{Nd}_{0.67}\text{Ca}_{0.33}\text{MnO}_3$	23
1-4 Lifting of the e_g orbital degeneracy of LaMnO_3 by Jahn-Teller distortion.....	24
2-1 Phase diagram of two manganites LCMO and PCMO.....	29
2-2 Resistivity as a function of temperature in LPCMO thin film of 300 Å thickness grown on NGO (110) substrate and LCMO grown on LAO.	30
2-3 Temperature dependence of the phase separated domains in $\text{La}_{0.33}\text{Pr}_{0.34}\text{Ca}_{0.33}\text{MnO}_3$ (LPCMO) grown on NGO (110) substrate as seen by magnetic force microscopy (MFM).....	31
2-4 Resistivity as a function of temperature of the LPCMO grown on LAO substrate.....	32
3-1 Pulsed laser deposition system.....	39
3-2 X-ray diffraction peaks of the film $(\text{La}_{0.5}\text{Pr}_{0.5})_{0.67}\text{MnO}_3$ grown on NGO substrate.....	40
3-3 Atomic force microscopy image of $(\text{La}_{1-y}\text{Pr}_y)_{0.67}\text{Ca}_{0.33}\text{MnO}_3$ with $y=0.5$	41
3-4 An AFM image of a 1000 Å thick film of $(\text{La}_{0.5}\text{Pr}_{0.5})_{0.67}\text{MnO}_3$, grown on STO (001) substrate.	42
3-5 Magnetization as a function of temperature in a thinner (75 Å) strained LPCMO film grown on STO substrate.....	43
3-6 Two different methods of measuring resistivity. (a) 4-probe method (b) 2-probe method.....	44
3-7 Resistance (R) as a function of temperature (T) of $\text{La}_{0.67}\text{Mn}_{0.33}\text{MnO}_3$ for various oxygen pressure.	45
3-8 Magnetization as a function of applied magnetization in $(\text{La}_{0.4}\text{Pr}_{0.6})_{0.67}\text{MnO}_3$ grown on NGO substrate.....	46
4-1 Resistivity vs. temperature curves for thin films of $(\text{La}_{1-y}\text{Pr}_y)_{0.67}\text{Ca}_{0.33}\text{MnO}_3$ ($y=0.4, 0.5, \text{ and } 0.6$) on NGO substrates.	56
4-2 Phase diagram of LPCMO created by using R vs. H isotherms.	57

4-3	<i>I-V</i> curves of the $(La_{1-y}Pr_y)_{0.67}Ca_{0.33}MnO_3$ ($y=0.6$) thin film in the cooling cycle with the voltage being ramped up.	58
4-4	<i>T-V</i> phase diagram for the $(La_{0.4}Pr_{0.6})_{0.67}Ca_{0.33}MnO_3$ thin film in the cooling cycle.....	59
4-5	<i>I-V</i> curves of the $(La_{1-y}Pr_y)_{0.67}Ca_{0.33}MnO_3$ ($y=0.6$) thin film in the warming cycle with the voltage being ramped up.	60
5-1	Current as a function of applied voltage in $(La_{0.4}Pr_{0.6})_{0.67}Ca_{0.33}MnO_3$	68
5-2	Magnetization as a function of magnetic field for three different voltages applied on $(La_{0.4}Pr_{0.6})_{0.67}Ca_{0.33}MnO_3$	69
5-3	Schematic of the manipulation of metallic domains by using electric field.....	70
5-4	Resistance and cross bar structure	71
5-5	Schematic of transverse resistance (R_T) measurement while the dc voltage is being applied in longitudinal direction.	72
5-6	Longitudinal resistance (R_L) and the transverse resistance (R_T)	73
6-1	Schematic of scanning of STM tip in constant current mode.....	83
6-2	Schematic of the STM spectroscopic tunneling.....	84
6-3	Design of different parts of the STM head	85
6-4	Voltage pulses in coarse approach mechanism.....	86
6-5	Current to voltage converter circuit for STM.	87
6-6	Feedback circuit for STM imaging. The proportional and Integral circuit are used.	88
6-7	Summing circuit for the input of piezoelectric scanner.....	89
6-8	A vacuum can and a probe to hold the STM head.....	90
6-9	Vibration isolation system	91
6-10	Scanning tunneling microscopy flow chart and electronics	92
6-11	Calibration scan on graphite at room temperature.....	93
6-12	Scanning tunneling Potentiometry circuit diagram.....	94

Abstract of Dissertation Presented to the Graduate School
of the University of Florida in Partial Fulfillment of the
Requirements for the Degree of Doctor of Philosophy

MANUPULATING THE MAGNETIC DOMAINS OF HOLE-DOPED MANGANITES BY
USING ELECTRIC FIELD

By

Tara P. Dhakal

May 2008

Chair: Amlan Biswas
Major: Physics

The observation of colossal magnetoresistance (CMR) and phase coexistence in hole-doped rare earth manganese oxides (manganites) have sustained the interest in these materials for over a decade. In recent years giant magneto resistance (GMR) materials have got recognition in the field of nanotechnology such as read/write memory devices. Because of the ever increasing demand of memory devices, researchers and engineers are compelled to look for new materials and reduce the device sizes even further. We investigate on the nanometer-sized phases coexisting in these manganites by using magnetotransport and scanning tunneling microscopy (STM) measurements. As thin films are required for industrial applications, we have grown thin films of manganites by using pulsed laser deposition on various substrates to obtain diverse physical properties. We will present the temperature dependence of the in-plane resistivity and the current to voltage (I - V) characteristics of these materials. While cooling and warming, resistivity of the manganites we grew shows hysteresis which is a signature of first order phase transition and phase coexistence.

We will present an unconventional method (magnetic field being conventional one) to tune one phase over another by applying electric field. This method is unique in that it can be applied precisely to the local phases unlike magnetic field which affects the whole region of application.

In an attempt to identify the different phases, we were able to draw a simple but unique phase diagram by using resistance vs. magnetic field ($R-H$) isotherms. The phase diagram contains two clean phases (metallic and insulator) and two mixed phases (static phase and fluid phase). Our results show a visibly distinct effect of the applied electric field in the region of the phase diagram where it is fluid phase. We call this fluid like phase an *electric soft matter* state. Our data suggest that the applied electric field orients the metallic domains of the material in the direction of the applied field. Using this electric field driven orientation we have been able to suggest a method to manipulate the magnetic nanostructure of manganites. In addition we will also attempt to obtain a local electronic picture of the material by using a technique called scanning tunneling potentiometry.

CHAPTER 1 INTRODUCTION

The unique properties of hole-doped manganese oxides (manganites) have generated great interest both due to the challenges they pose to our understanding of fundamental magnetic phenomena and because they show prospect of application in new device technologies [1-4]. Manganites show a sharp insulator to metal transition (I-M) as a function of several factors like temperature, electric field, magnetic field, light, hydrostatic pressure, strain etc [5-10]. The transition due to a magnetic field leads to a colossal magnetoresistance (CMR) in manganites. The *I-M* transition is also accompanied by a paramagnetic to ferromagnetic transition as the temperature is lowered. In addition the transition also brings about a structural change in the material. Thus the physics of manganites is dictated by the interplay between the magnetism, the electronic properties and the lattice structure. Due to this complexity, manganites exist in various phases important for fundamental physics and technological aspects as well. As giant magnetoresistance (GMR) materials have already made their way to the real life applications [11-13], the CMR materials show a bright prospect for device technology.

Double Exchange Mechanism

Manganites have a chemical formula $RE_{1-x}AE_xMnO_3$ where RE is a rare earth ion like La, Pr, Nd etc. and AE is a divalent ion like Ca, Sr, and Pb etc. These materials show colossal magnetoresistive (CMR) effect and an insulator to metal (*I-M*) phase transition. In the undoped limit where $x=0$ (zero) the material is an antiferromagnetic insulator. In this case the Mn^{3+} ions have 4 electrons in the $3d$ -shell, and they are surrounded by O^{2-} , forming an octahedron. The crystal field splits the d -orbitals into 2 e_g and 3 t_{2g} orbitals. Hund's coupling favors that 3 electrons populate the t_{2g} orbitals and 1 electron the e_g orbitals. The t_{2g} electrons are localized and e_g electrons become itinerant above a certain critical doping and use oxygen p orbitals as a

bridge between Mn ions. Furthermore in the undoped case e_g degeneracy is split due to Jahn-Teller (JT) distortion. This splitting localizes the e_g electrons thus making the undoped material an insulator. In this case the energy is minimized if the spin alignment is antiferromagnetic.

On the other hand a ferromagnetic metallic phase is formed in the composition range $0.2 < x < 0.5$ [3]. The strong ferromagnetic behavior of these hole-doped manganites is a consequence of the double exchange mechanism (DE) [14-16]. The divalent AE ions when doped in place of the trivalent RE ions results in the mixed valency of the transition metal ions, $Mn^{3+} (t_{2g}^3 e_g^1)$ and $Mn^{4+} (t_{2g}^3 e_g^0)$. For example, if 20% of the RE^{3+} cations were replaced by AE^{2+} cations then 20% of manganese ions have to be Mn^{4+} instead of Mn^{3+} to match valency proportion. Since there are no electrons in the e_g level of Mn^{4+} , the e_g electron of an Mn^{3+} ion will hop to the neighboring Mn^{4+} ion via double exchange thus giving rise to conductivity in these materials. This DE of Mn^{3+} and Mn^{4+} occurs only if the spin of the respective d -shells align parallel to each other as shown in figure 1-1. In un-doped case, the super exchange interaction gives antiferromagnetism.

Crystal Structure of the Manganites

The manganites have the ABO_3 (here $A=RE_{1-x}AE_x$ and $B=Mn$ for the present manganites) type of perovskite structure. As can be seen from the figure 1-2 (a), the smaller manganese ions form a cubic lattice with the larger RE (La, Pr, etc.) ions at the body center. The ionic radii of La, Pr, etc are shown in table 1-1. The oxygen ions are located at the centers of the cube edges. If we look at the bottom right of the figure 1-2 (c) we see that the Mn ion is surrounded by six equidistant oxygen atoms to form a regular MnO_6 octahedron.

The MnO_6 octahedron and its 3-D network in perovskite structure when repeated in space is shown in figure 1-2 (c). Among the octahedra or at the corners of the cubes lie the trivalent rare earth (RE) and/or divalent alkaline earth (AE) cations which have relatively larger ionic radii (see table 1-1). The Mn ions which are at the center of each octahedron and the oxygen ion

at the corners are not shown on the figure 1-2 (c). The properties of the perovskite structure compounds can be controlled by cation substitution and/or oxygen stoichiometry. The substitution of cation actually may rotate the MnO_6 octahedra and therefore the whole structure may not look like ideal cube as shown in the figure 1-2 (b).

The ability to tune such distortion helps us to understand the co-relation among magnetic, structural and electronic degrees of freedom in the transition metal oxides. In the case of CMR oxides like manganites the perovskite structure is in fact strongly distorted by the combined effect of lattice mismatch (tolerance factor¹) and electron instability (Jahn-Teller distortion to be explained in a latter section).

Colossal Magnetoresistance, I-M Transition and Magnetism

The colossal magnetoresistance (CMR) which is a huge reduction of resistivity of the material by the application of a magnetic field is one of the most stimulating phenomena observed in manganites in the hole-doping range of 20 to 50% [17]. The term colossal is because of the fact that the negative magnetoresistance (MR) found in these materials are sometimes close to 100 %. The MR in this case is defined such that the maximum value of MR would never exceed negative 100 % as seen below in the following equation.

$$MR = \frac{\rho_H - \rho_0}{\rho_0} \times 100\% \quad (1-2)$$

¹ The tolerance factor is defined as

$$\tau = \frac{d_{R-O}}{\sqrt{2}d_{Mn-O}} \quad (1-1)$$

where d_{R-O} and d_{Mn-O} are average RE cation-oxygen and manganese-oxygen distances. A tolerance factor $\tau = 1$ characterizes an unstrained cubic perovskite and $\tau < 1$ or $\tau > 1$ represents a strain which is relaxed by distorting the structure away from the cubic form.

where ρ_H and ρ_0 are the resistivities at applied and zero magnetic fields respectively.

In the same composition range as mentioned above, a peak is seen in the resistivity at a temperature usually symbolized by T_p . Such an evolution of resistivity is a characteristic of an insulator to metal ($I-M$) transition with decreasing temperature.

Figure 1-3 shows such a graph showing both $I-M$ transition and CMR effect for a single crystal of $\text{Nd}_{0.67}\text{Sr}_{0.33}\text{MnO}_3$. The peak in resistivity is accompanied by a magnetic transition at the Curie temperature (T_c). Below T_c the material is a ferromagnetic metal (FMM) and above T_c , it is a paramagnetic insulator (PMI). These type of transitions can be explained by C. Zener's DE [14] mechanism. In reference [14], he has established a quantitative relation between the electrical conductivity (σ) and ferromagnetic Curie temperature (T_c).

$$\sigma = \left(\frac{xe^2}{ah} \right) \left(\frac{T_c}{T} \right) \quad (1-3)$$

where x is composition of a divalent cation (AE) to be doped in the trivalent rare earth cation (RE), e is the electronic charge, a is the lattice parameter, h is Planck's constant and T is temperature.

The relation (1-3) agrees excellently with the compound $\text{RE}_{1-x}\text{AE}_x\text{MnO}_3$ with RE = La, Nd and AE = Ca, Sr, or Ba studied by Jonker and Van Santen [17] and many others in the composition range $0.2 < x < 0.5$ for the temperatures well below the curie temperature (T_c). Because of the creation of a hole on the Mn^{4+} site an electron from $\text{Mn}^{3+} e_g$ band can easily hop to the hole in the Mn^{4+} site via O^{2-} ion and vice versa with strong on site Hund's coupling. Below T_c hopping of the electron and in turn the FM state is enhanced if the relative spins of the d -shell electrons are parallel. But when the temperature is up to near or above T_c the spin alignment gets disordered and eventually the hopping interaction is reduced on average. At this point if we

apply the magnetic field to the material, the spin disorder is reduced pushing T_p toward higher temperature and therefore a large MR is expected around T_c . This is a naive description attempted to explain CMR effect by DE interaction. However the DE theory (cf. the relation (1-3)) can not explain the higher temperature transport properties and the CMR effect quantitatively. At high temperatures since the spins are all oriented in random directions, the e_g electron of Mn^{3+} ion can not hop to Mn^{4+} as allowed by double exchange. This e_g electron then has to be thermally activated to be able to drag or distort the embedded lattice with it [3, 18]. So the hopping now occurs at the cost of the neighboring lattice distortion or in other words the polaron formation. This distortion now lowers the energy of the one e_g electron of Mn^{3+} and localizes the electron within itself. This is why this material is insulating at high temperature. However as the temperature is increased the electron is activated to hop carrying the polaron[19, 20] with it. The activated electric conductivity has the form

$$\sigma(T) \propto \frac{1}{T} \exp(-E_a / k_B T) \quad (1-4)$$

Here E_a is the small polaron hopping energy which is approximately half of the polaron binding energy [3]. In some manganite, it shows a good fit with \sqrt{T} instead of T in equation (1-4) [21]. This effect is known as the polaron hopping model. Variable range hopping (VRH) type of expression also holds good above T_c but the characteristic temperature is found to have physically unrealistic values [1]. The thermoelectric power, as in a semiconductor, is proportional to $1/T$, but the characteristic energy is much smaller than E_a [3]. Thus the polaron hopping model described above is the best model so far to describe the transport behavior of the paramagnetic insulator (PMI) region (above T_c) of a manganite of the form $RE_{1-x}AE_xMnO_3$ with $RE = La, Nd$ and $AE = Ca, Sr, Ba$.

The DE is not sufficient to explain CMR observation even at low temperatures. At low temperature when the magnetization is near saturation the resistivity does not decrease anymore and one can expect, as explained by DE, that MR tends to zero as T tends to zero. However, contrary to this, MR at 4T has been found around 35% which increases as T tends to zero in the compound $\text{La}_{0.75}\text{Ca}_{0.25}\text{MnO}_3$ [22].

Jahn Teller Distortion

The physics of manganites looks very complex. To explain these complexities, we need other mechanisms besides DE. Some of them are based on electron-lattice interaction, antiferromagnetic super exchange interaction between the t_{2g} local spins, orbital ordering tendency between the e_g orbitals etc. The important electron-lattice interaction arises from the Jahn-Teller type [23, 24] lattice distortion. The distortion stems from an electronic instability inherent to the Mn^{3+} ion in an octahedral crystal field. Under the influence of the weak crystal field, Mn^{3+} , which has 4 d -electrons adopts a high-spin configuration with 3 electrons in t_{2g} orbitals and 1 electron in the e_g orbital. This single electron in the e_g orbital is in the orbitally degenerate state. Such an orbitally degenerate state is unstable to a distortion and thus is relaxed by lifting the degeneracy.

Figure 1-4 shows a schematic of how the e_g band of LaMnO_3 is split by Jahn-Teller (JT) distortion to make the material insulating. This Jahn-Teller distortion splits the e_g orbitals by around 1.5 eV [25]. LaMnO_3 is not only JT distorted but also orbital-ordered [26-29]. Its spin ordering structure is A -type in which the ferromagnetic ab plane is coupled antiferromagnetically along the c -axis. Such a distortion can be caused by the reduced size of the rare earth ion that occupies the A site of ABO_3 (in our case A is (RE, AE) and B is Mn) structure because it gives rise to a rotation of the MnO_6 octahedra in order to fill the empty space created. It has been found

that around 20% of hole doping i.e. creating that much of Mn^{4+} removes the orbital degeneracy and thus the structural distortion². The other factors that may cause the distortion are the strain caused by the substrate in case of thin films and external perturbations like temperature.

Other types of materials that exhibit CMR properties are in the composition range, $x \sim 0.5$. These kinds of manganites show two transitions PMI-FMM and FMM-AFMI with lowering temperatures. In the PMI-FMM transition a peak in resistivity is observed, at a temperature that coincides with the Curie temperature (T_c). The FMM-AFMI transition, which takes place at Neel temperature (T_N), corresponds to the existence of charge ordered insulating state (COI) below $T_{CO} \approx T_N$, where T_{CO} is the temperature at which charge ordering takes place. This effect is due to the fact that in these types of manganites, the Mn^{3+} and Mn^{4+} species are in equal amounts and tend to order more easily [22, 30, 31]. In addition the manganites above $x=0.5$ also show charge ordering. The Mn^{3+} and Mn^{4+} are found to be ordered as thin stripes in $\text{La}_{0.33}\text{Ca}_{0.67}\text{MnO}_3$ [32].

There are other type of manganites which are phase separated. Due to the comparable free energies of the COI and FMM phases, certain manganites display phase separation in which, the micrometer sized FMM and COI regions are observed to coexist at certain temperatures (see chapter 2). We are mainly interested in these phase separated manganites.

² It should be noted that the Mn^{4+} ion is Jahn-Teller inactive since it has no unpaired electron in e_g orbital.

Table 1-1: Ionic radii of different ions in LPCMO manganite.

Ions	Radii (\AA)
La^{3+}	1.17
Pr^{3+}	1.13
Ca^{2+}	1.14
Mn^{3+}	0.75
Mn^{4+}	0.67
O^{2-}	1.24

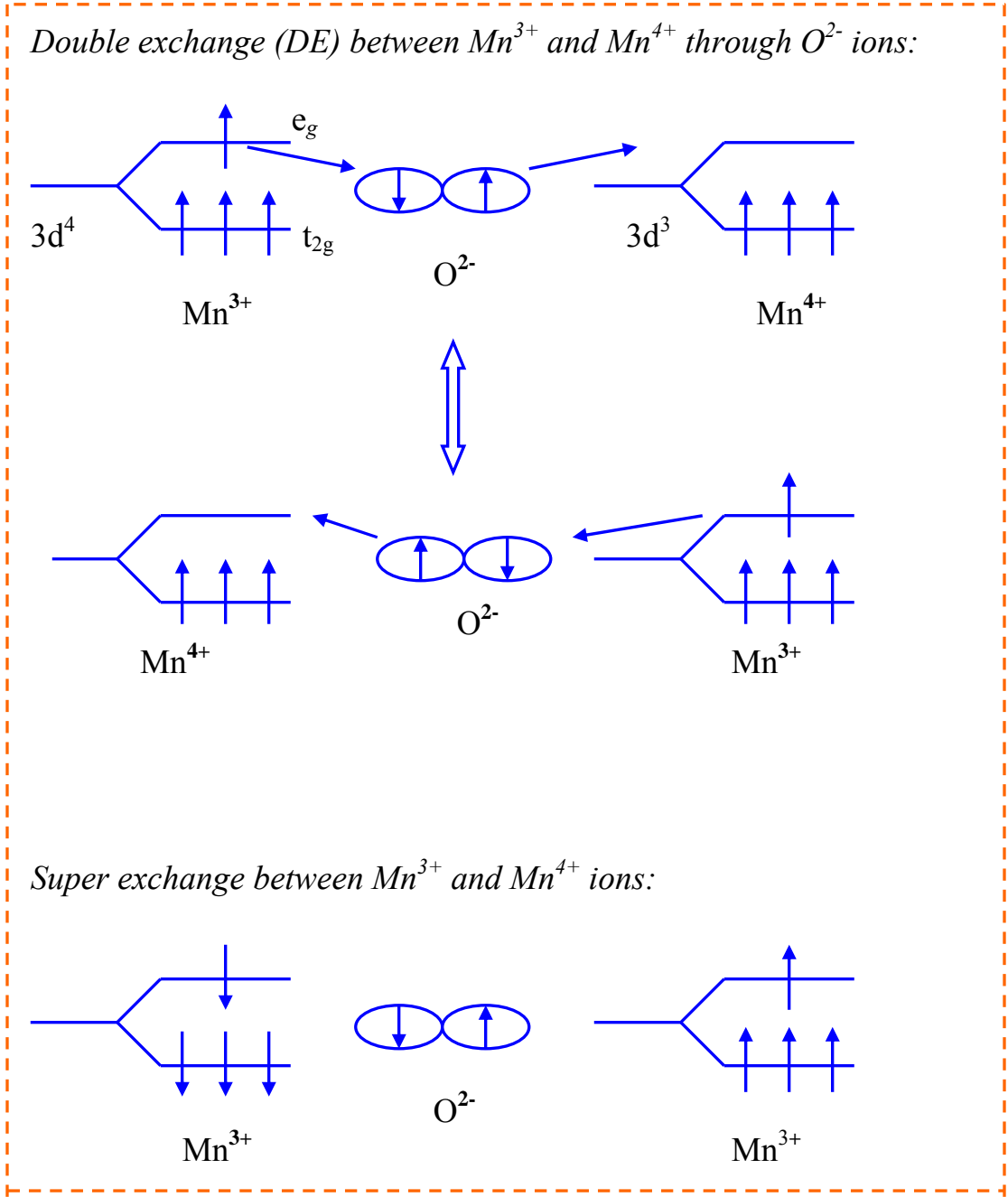


Figure 1-1: Double exchange of e_g electron in two Mn sites via oxygen $2p$ state. The DE is possible only if the moments of the two cations are parallel. The super exchange interaction aligns the moments antiparallel.

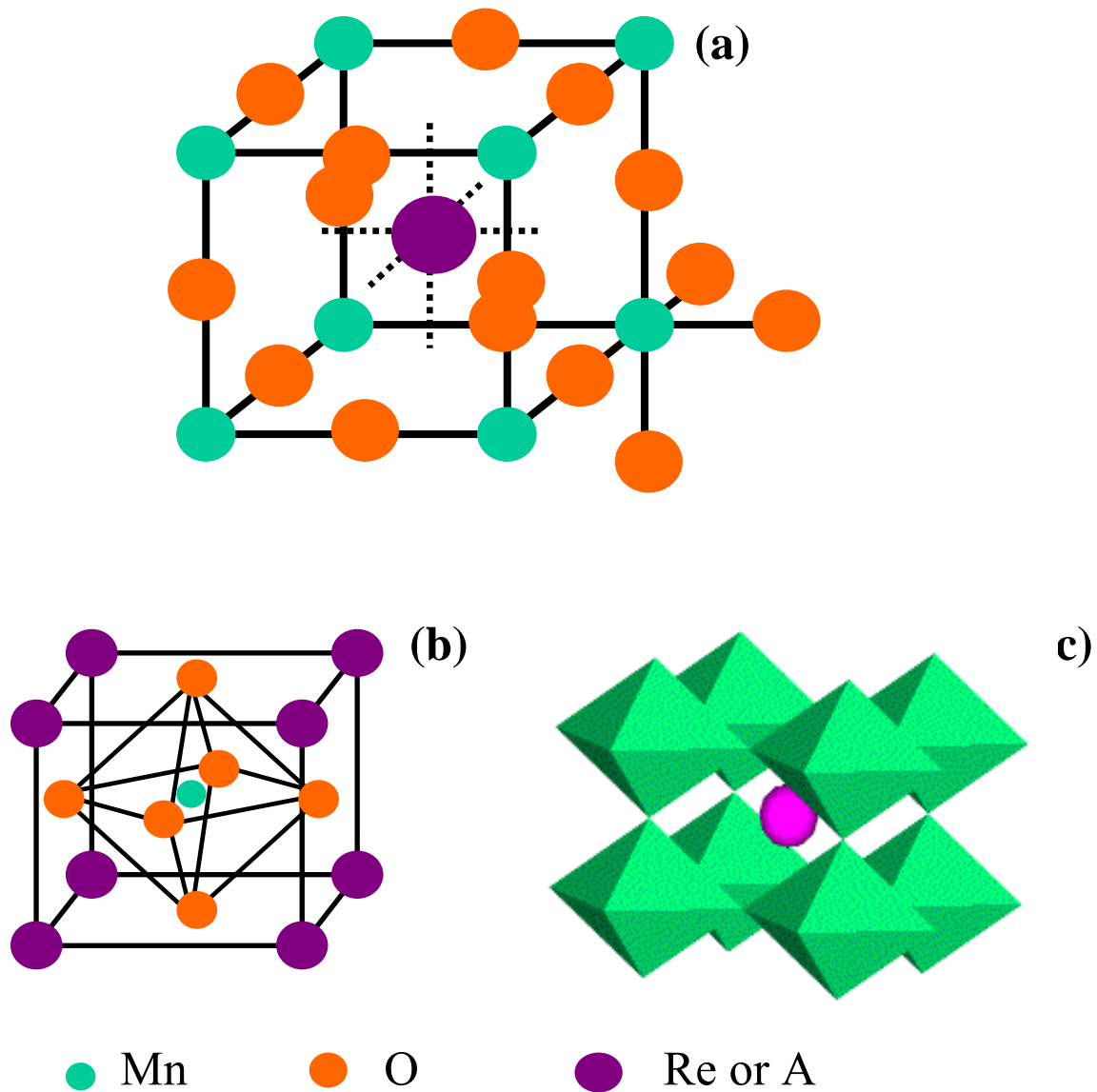


Figure 1-2: Structure of the manganites with perovskite lattice. (a) Mn ions can be seen surrounded by six oxygen ions. (b) RE ions shown on the corner of a cube which contains oxygen octahedron with Mn ion at its center. (c) Network of corner-sharing MnO₆ octahedra in the perovskite structure.

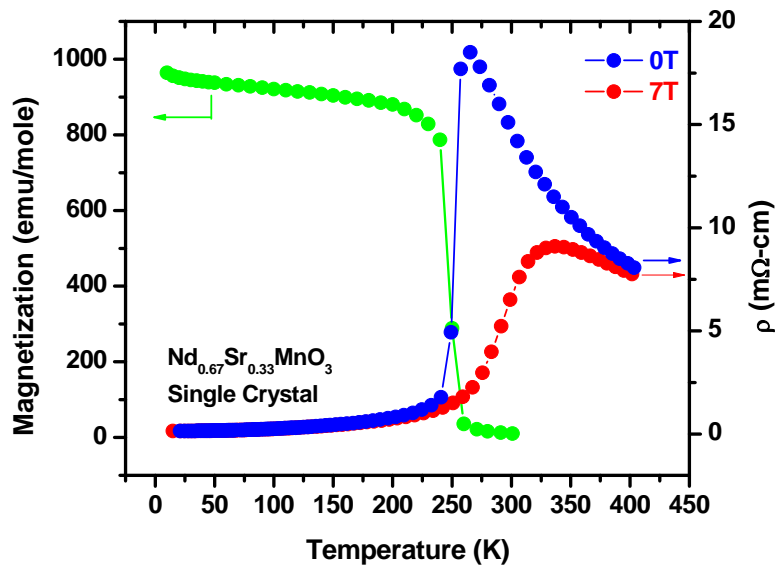


Figure 1-3: Reduction of resistivity by a magnetic field as a function of temperature in the compound $\text{Nd}_{0.67}\text{Ca}_{0.33}\text{MnO}_3$. This sample shows an metal-insulator transition around 265 K for zero field. The magnetoresistance (MR) at 7T is around 90% at peak temperature. The magnetization curve (green) shows that the magnetic transition occurs around the I - M transition.

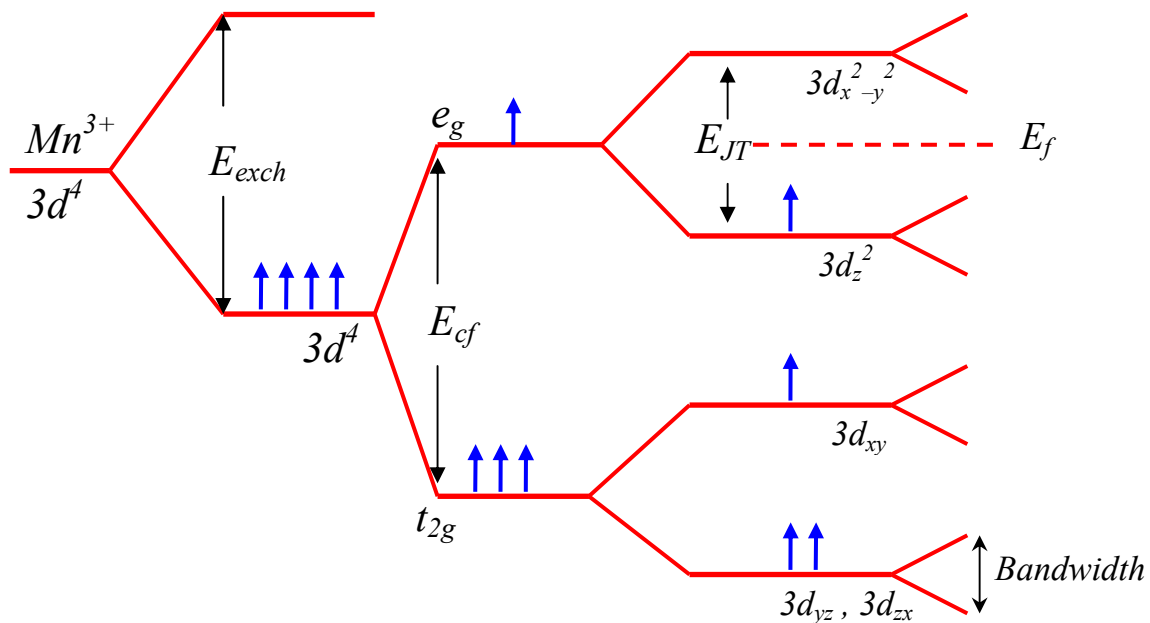


Figure 1-4: Lifting of the e_g orbital degeneracy of $LaMnO_3$ by Jahn-Teller distortion. The values of exchange field (E_{exch} , the weak crystal field (E_{cf}) and the E_{JT} are found to be around 3 eV, 2 eV and 1.5 eV respectively. The Fermi level is in the middle of the Jahn-Teller split labels. The bandwidth is around 1.5 to 2 eV. [25, 26].

CHAPTER 2 PHASE COEXISTENCE IN MANGANITES: PR SUBSTITUTION

It has been found that a diverse range of electronic and magnetic phases coexist in manganites [33, 34]. The coexistence of such phases is due to the competition between double exchange (DE) and Jahn-Teller effect [35]. Figure 2-1 shows the phase diagram of two manganites $\text{La}_{1-x}\text{Ca}_x\text{MnO}_3$ (LCMO) and $\text{Pr}_{1-x}\text{Ca}_x\text{MnO}_3$ which have different ground state (GS) at the same carrier density. For example in the composition range $x=0.33$ where $\text{La}_{1-x}\text{Ca}_x\text{MnO}_3$ is ferromagnetic metallic (FMM), $\text{Pr}_{1-x}\text{Ca}_x\text{MnO}_3$ is a charge ordered insulator (COI). We want to destabilize the GS of one by mixing with the other. So by mixing these two manganites together we expect to observe phase coexistence. The chemical composition of the compound thus produced, which is our material under study, is: $(\text{La}_{1-y}\text{Pr}_y)_{0.67}\text{Ca}_{0.33}\text{MnO}_3$ (where $y = 0.4, 0.5$ and 0.6) (LPCMO). Such phase coexistence in fact has been observed by us and other groups [6, 5]. In the latter chapter our results on electric field effect on LPCMO will be presented.

The coexistence of FMM and COI phases has also been found in strained thin films, for example, $\text{La}_{0.67}\text{Ca}_{0.33}\text{MnO}_3$ (LCMO) at low temperatures [9, 36]. In the thin films of this material grown on LaAlO_3 (LAO) substrates, a compressive lattice mismatch strain leads to 3-D island growth and hence a non-uniform distribution of strain in the film. The high strain regions of the film are converted to the COI state while the low strain regions remain in the FMM state. Such a phase-separated state is confirmed using low-temperature magnetic force microscopy (MFM) [37, 38] and magneto-transport measurements. This phase separated state is not observed in the bulk form of this compound and is caused by the structural inhomogeneities due to the non uniform distribution of strain in the film. Thus it was a clear evidence of the strain induced charge ordered state. The strain weakens the low-temperature ferromagnetic metallic state and a charge-ordered insulator is formed at the high strain regions. This conclusion was drawn because the

sample magnetization shows ferromagnetism where as the resistivity measurement under same conditions shows insulator like behavior. It is only possible if FMM and COI phases coexist. However, as the films were grown thicker, the transport properties of LCMO thin films approached that of the bulk.

We would like to investigate if the phase coexistence in LPCMO manganites is solely due to the Pr substitution. We have seen that as the Pr content is lowered, the FMM state becomes the dominant phase at low temperatures. This is analogous to the behavior of LCMO under substrate induced strain. However, the observed hysteresis in the LPCMO ρ vs. T (as shown in figure 2-2 a) is conspicuously absent in the ρ vs. T data of the strained LCMO (figure 2-2 b). This gives a hint about the origin of phase separation for the two cases. When the phase separation is due to substrate induced strain the two phases are locked to the strain landscape of the thin film produced due to the 3-D island growth. It is conceivable that for LPCMO the strain landscape is not predetermined and is dictated by the martensitic transition at low temperatures. To check this hypothesis we grew thin films of LPCMO on NGO substrates to minimize the lattice mismatch strain. The first direct evidence of the formation and evolution of these phase separated regions in thin films of LPCMO [19] was seen by Zhang *et al.* They used low temperature magnetic force microscopy (LTMFM) to image the magnetic domain structure of these films. As temperature is lowered from high temperature, the ferromagnetic domains were seen to form and grow as if they were fluid (figure 2-3).

The broad hysteresis in resistivity of LPCMO is attributed to phase coexistence and the sharp transition to the first order nature of the transition. To explain what causes the mixed phases in our LPCMO manganite we have to consider both the substrate induced strain and the effect of Pr-content. As we know the COI phase and FMM phase are structurally different, the

former being pseudo-tetragonal and the latter being pseudo-cubic. In thin films the built in strain due to the lattice mismatch between the substrate and the material introduces a structural distortion, which in turn suppresses the FMM phase. As has been seen in LCMO by Biswas *et al.* [9, 36], the metallic region observed on LCMO grown on NGO substrate is turned into insulating state when grown on LaAlO_3 (LAO) (001) substrate. Note that LAO unlike NGO has different lattice parameters compared to LCMO, so it introduces higher strain (about 2% compressive strain). Our sample is grown on NGO (110) so we expect a minimal substrate induced strain effect (0.52%). Now since Pr has smaller cation radius than La, it distorts the cubic perovskite structure of the LCMO. This distortion actually now creates a high strain region in the material pinned on the Pr-site. This strain effect appears, at least through experimental results, fundamentally different from the effect of the substrate induced strain. The sharp transition and the hysteresis are signatures of phase coexistence in LPCMO whereas LCMO grown on LAO does not show such behavior. LPCMO grown on LAO also shows that the transition broadens, moves toward lower temperature and the hysteresis width shrinks significantly as shown in figure 2-4. So in our material Pr has a big role to play. In LCMO grown on LAO the strained region is dominant only on the interface between the substrate and the material whereas in LPCMO the strain, although pinned at Pr-sites, spreads throughout the material.

In addition, in thin films the substrate-induced strain does not allow the bulk structural transition to occur. However what we saw is that our resistivity drop is very sharp similar to what is observed in the bulk forms of the material. The kink on the resistance observed on the bulk LPCMO manganite when the material goes from paramagnetic insulator (PMI) state to the COI state [6] is also absent in our thin film sample. We believe that the Pr cations first introduce a built in strain landscape at the high thin film deposition temperatures (820°C). As the sample is

cooled below the charge ordering temperature, the COI phase is formed in the high strain regions. The PMI phases formed at low strain region remain as PMI phases even below the charge ordering temperature because the structural transition is prevented in thin films. This removes the resistivity anomaly at the PMI to COI transition temperature. In addition, the strain landscape is modified due to thermal contraction of the substrate. As the temperature is lowered further, the FMM phase is nucleated at the low strain regions. The FMM and COI phases then follow the strain landscape as the temperature is lowered until at the lowest temperatures a major fraction of the film goes to the FMM state, which is reminiscent of martensitic transformation. And because the lattice constants of the NGO substrates closely match the lattice constants of the low temperature FMM phase, the low temperature resistivity of our thin films is lower than that of bulk LPCMO of similar composition. Hence, a large-scale phase separation is observed in thin films of LPCMO, which exhibit transitions similar to those observed in single crystals. The fact that we have been able to achieve such sharp transitions in thin films of LPCMO is therefore significant for understanding the underlying mechanism of colossal magneto-resistance (CMR) and phase separation. In addition this is also an important step towards possible future applications of this phenomenon since thin films would be required for use in devices.

The experiments described in the following chapters are designed to test the hypotheses outlined above. The sample growth, characterization, transport and surface measurements, and the conclusions drawn are described in detail.

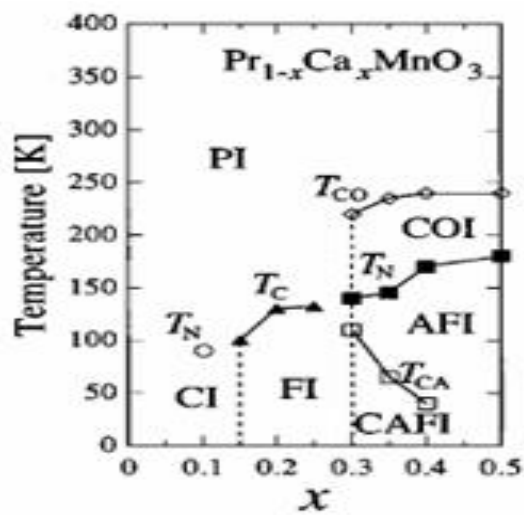
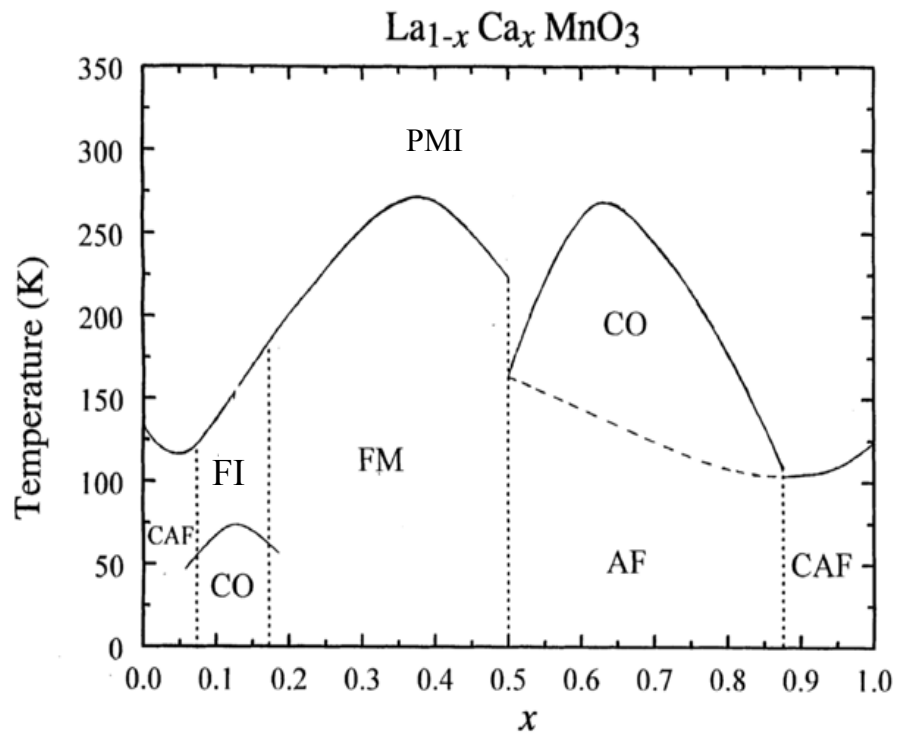


Figure 2-1: Phase diagram of two manganites LCMO (upper panel) and PCMO (lower panel [24, 39]).

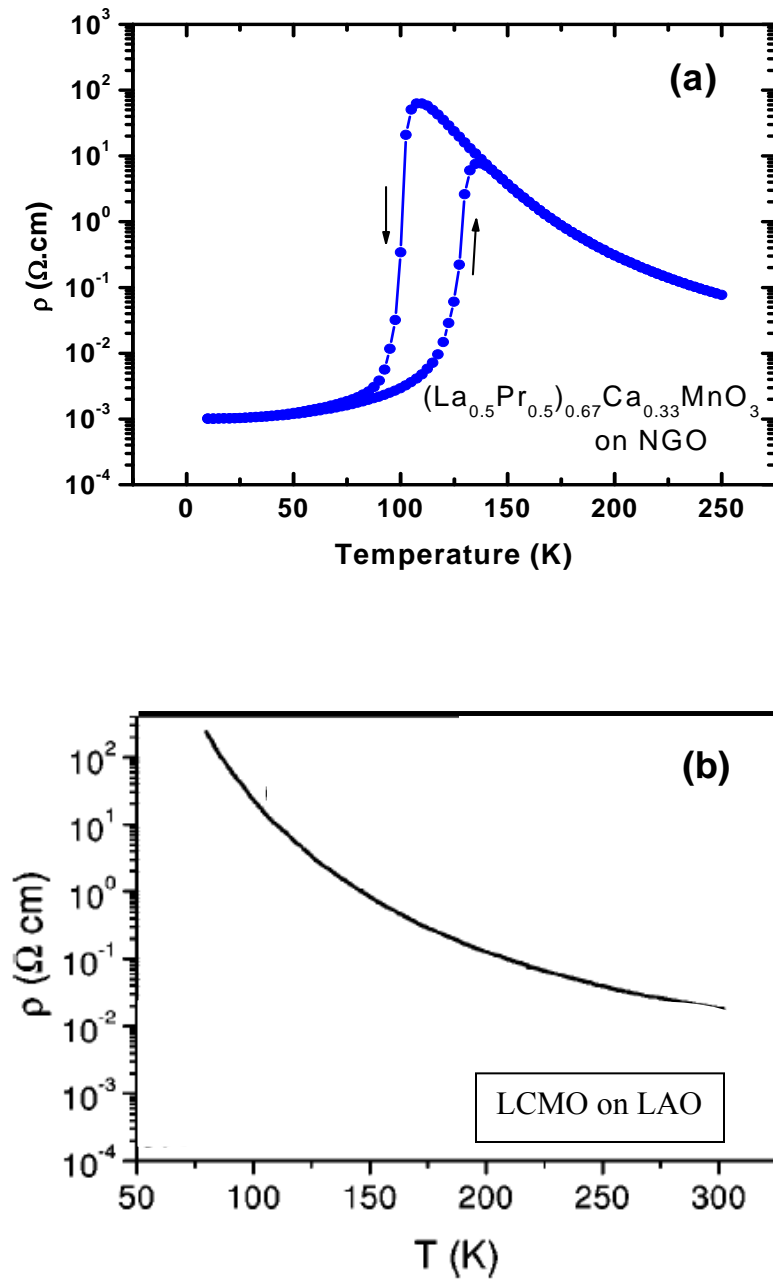


Figure 2-2: Resistivity as a function of temperature in LPCMO thin film of 300 Å thickness grown on NGO (110) substrate and LCMO grown on LAO. (a) The resistivity of LPCMO shows a broad hysteresis between warming and cooling cycles of temperature shown in the graph by arrows. The broad hysteresis and the sharp transitions are attributed to first order type of transition. (b) The resistivity as a function of temperature for $\text{La}_{0.67}\text{Ca}_{0.33}\text{MnO}_3$ (LCMO) grown on LaAlO_3 (LAO) (001) substrate. The thickness of the film is 150 Å.

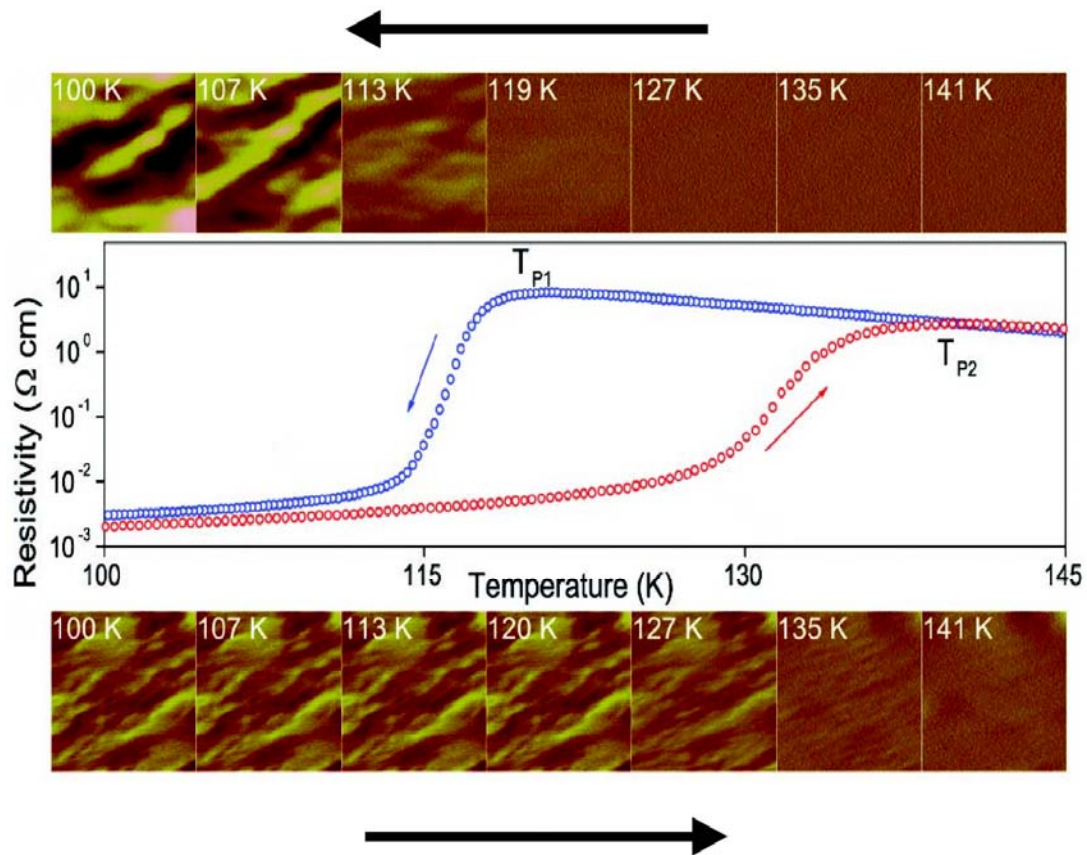


Figure 2-3: Temperature dependence of the phase separated domains in $\text{La}_{0.33}\text{Pr}_{0.34}\text{Ca}_{0.33}\text{MnO}_3$ (LPCMO) grown on NGO (110) substrate seen by magnetic force microscopy (MFM). The middle panel shows the resistivity behavior of the film. The upper panel shows the cooling run and the images are $6\mu\text{m} \times 6\mu\text{m}$ and the lower panel shows the warming run and the images are $7.5\mu\text{m} \times 7.5\mu\text{m}$ [5].

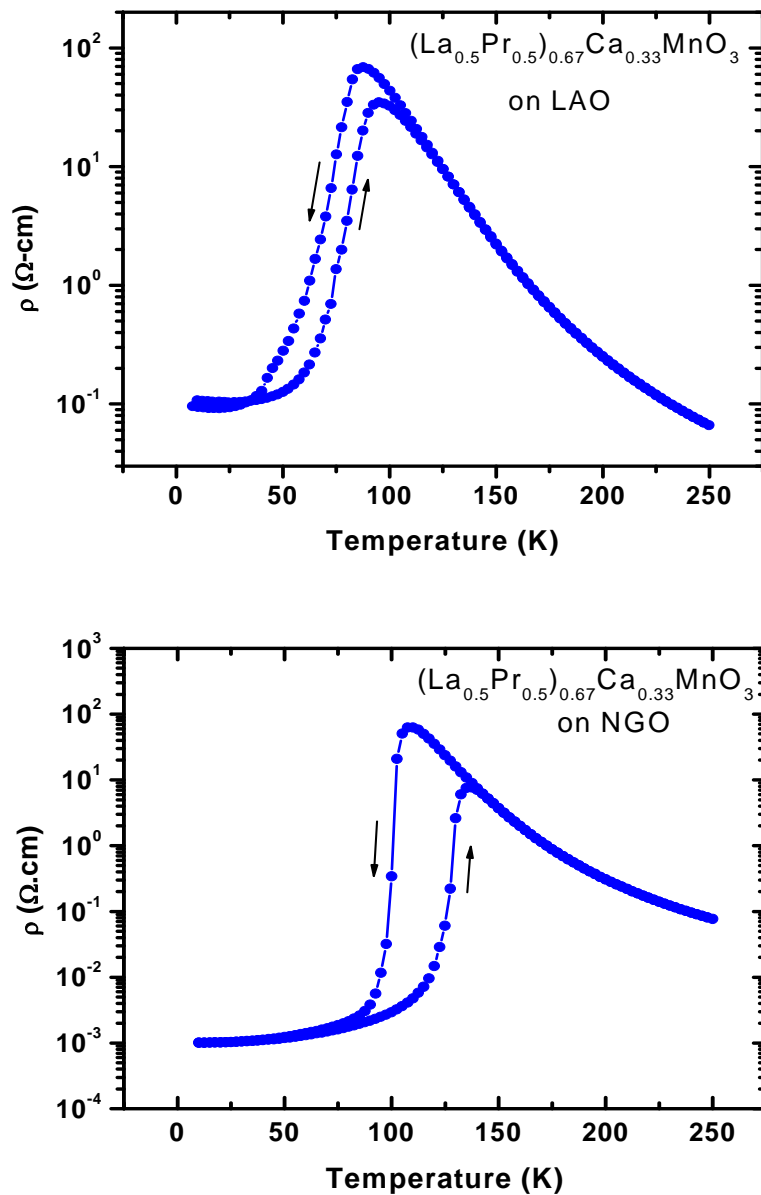


Figure 2-4: Resistivity as a function of temperature of the LPCMO grown on LAO substrate. For comparison, the LPCMO grown on NGO is reproduced from figure 2-2 (a) on the lower panel. The arrows show the direction of the temperature sweep.

CHAPTER 3 MATERIALS AND EXPERIMENTAL METHODS

Three compositions of $(\text{La}_{1-y}\text{Pr}_y)_{0.67}\text{Ca}_{0.33}\text{MnO}_3$ with $y=0.4, 0.5,$ and 0.6 have been used to study the electrical transport and magnetic properties of this materials. As our focus was on the physics associated with the basic properties of these materials as well as the search for the possible technological applications, thin films were grown on different substrates. The substrates used were NdGaO_3 (NGO) (110), SrTiO_3 (STO) (100) and LaAlO_3 (LAO) (100) substrates (see table 3-1 for the strains for all the substrates on LPCMO).

Pulsed Laser Deposition

Thin films of the above materials were grown by using a technique called pulsed laser deposition (PLD) [40]. This PLD system was set up in our own laboratory. The laser used was 248 nm excimer laser. In the PLD process a pellet (target) of the desired composition is rotated while the laser pulses are made to hit the target at around 45° . The evaporated plume of the plasma is then directed toward the substrate which is positioned on the heater such that it is just at the center of the path of the evaporated plumes as shown in the figure 3-1.

Before optimizing the growth conditions, we had to play with parameters like pulse rate, pulse energy, oxygen pressure during the growth and after the growth. The sample conditions were optimized for sharper transitions and better conductivity. In figure 3-7, three different graphs of resistance vs. temperature are shown. All the three films were grown with different oxygen pressures during the growth and after the growth during cooling. As we can see that the peak temperature in resistance vs. temperature graph is very sensitive to the oxygen pressure. The oxygen pressures for sample # 1 during the growth and post growth were 420 mTorr and 450 Torr. The pressures for similar situations for sample #2 and sample # 3 were 520 mTorr and 475 Torr and 600 mTorr and 550 Torr

respectively. The substrate used was NdGaO₃ (NGO) (110) and the substrate temperature during growth 820°C for all three samples. The cooling rate was 20°C and the laser pulse repetition rate was 5 Hz. The pre-ablation was done for 5 mins with repetition rate of 10 Hz. The energy of the laser pulse was kept at 480 mJ. The arrows shown in the figure are for the peak temperatures for the R vs. T graph. The conditions used are valid only for La_{0.67}Ca_{0.33}MnO₃. For the manganite samples with other compositions, different sets of conditions had to be found. The optimized conditions are given in the following paragraph.

The substrate temperature during the growth is kept at 820°C. The films were grown at an oxygen pressure of 450 mTorr. The frequency of the laser pulse was kept at 5 Hz during the growth and 10 Hz during the pre-ablation. Before and after the growth the heating and cooling rates were kept at 20°C respectively. The oxygen pressure during post growth cooling was kept at 430 Torr.

Standard θ - 2θ x-ray diffractometry was used to check whether the samples grown are epitaxial and are of single chemical phase. The intensity of the x-ray peaks as a function of the angle of incidence is given in the figure 3-2 for the sample (La_{0.5}Pr_{0.5})_{0.67}Ca_{0.33}MnO₃. The arrows indicate peaks due to sample holder and S indicates substrate peaks. The film peaks are not clearly visible due to the nearly perfect lattice match with the substrate. The shallow region of graph on the lower panel of graph is due to the film. The tail on both sides of the substrate would look symmetrical if there was no film deposited on it. Additional techniques like magnetization and scanning probe microscopy were used to verify the best growth conditions which will be explained in latter sections.

Atomic Force Microscopy

Atomic force microscopy (AFM) was first discovered by G. Binnig *et al.* in 1986 [41]. Since then, AFM is widely used in material and biological sciences [42, 43]. After the films are

grown, we have used atomic force microscopy to see the surface roughness of the material. A commercial atomic force microscope from Digital Instruments was used to scan the samples of manganites grown. The commercial AFM is capable of scanning $12\mu\text{m}\times 12\mu\text{m}$ in one scan. We have also used it for magnetic force microscopy (MFM) of some of the manganites like $\text{La}_{1-x}\text{Sr}_x\text{MnO}_3$ which are ferromagnetic even at room temperature. An AFM image of a 75 \AA thick film of a mixed phase manganite grown on STO (100) substrate is shown in figure 3-3 a. The LPCMO films grown on the STO substrate are subjected to a tensile strain of 1.69% (table 3-1). Because of this high strain, manganites are grown as disconnected islands. However in the film grown on NGO, which has a low tensile strain of 0.59%, the manganite islands are grown as connected islands (figure 3-3 b). Both of these films were around 75 \AA thick. As is shown in figure 2-2 (a) of chapter 2, a 300 \AA thick film of LPCMO grown on NGO shows a hysteresis in resistance between the cooling and warming cycles of temperature and the transition from insulator to metal while cooling is very sharp like that in first order transition. However, a 300 \AA thick film grown on STO substrate is insulating all the way to lowest temperature. To see similar hysteretic behavior typical of LPCMO, we had to grow a film thicker until the islands started to overlap each other. In figure 3-4, an AFM image of a 1000 \AA film of LPCMO grown on STO substrate and its resistance as a function of temperature are shown. The AFM image clearly shows the overlapped islands and resistance shows the hysteresis typical of LPCMO manganites. We also wanted to confirm that the islands grown are ferromagnetic below the insulator to metal transition. For this we measured magnetization of a LPCMO film grown on STO and we chose the 75 \AA thick film where the islands are very well separated from each other. As shown in figure 3-5, the magnetization shows ferromagnetic behavior. Magnetization as a function of temperature is shown for both field cooled and zero field cooled case.

Transport Measurements

Transport measurements are extremely important for an experimental physicist. In addition to the simplicity of the techniques used, these measurements give a tremendous amount of information on the electronic and magnetic properties of the materials studied. For our sample with lower resistivity ($\rho=0, 0.4, \text{ and } 0.5$), a 4-probe method is used as shown in figure 3-6 (a). In this method, current (I) is passed through the 2 outside leads and voltage (V) is read from the remaining 2 internal leads as shown in the figure. The resistance of the sample (R_s) then would be V/I . In this method since current doesn't flow through the voltmeter (provided the impedance of the voltmeter is very high compared to the sample resistance), the contact resistance and the lead resistance are automatically excluded from the resistance measurement. For the sample with higher resistivity ($\rho=0.6$), a 2-probe method as shown in figure 3-6 (b) was used for the resistivity measurements. Here the current through the circuit would be $I=V_R/R$ and the voltage across the sample would be $V_s=V_0-V_R$. The sample resistance is $R_s=V_s/I$. By using this method we avoid connecting a voltmeter across the high resistance sample which is necessary because the input impedance of the voltmeter is comparable to the sample resistance around the peak resistance temperature.

Magnetization Measurements

For magnetotransport measurements a high field magnet system from American Magnetics was used. A dc magnetic field of 9T could be applied in this system and the temperature could be varied from 1.5K to 300K using a Janis Variable Temperature Insert. For data acquisition, National Instruments' Labview program was developed and used. For magnetization measurement a SQUID magnetometer was used which is a shared facility within the physics department. It is very hard to measure magnetization of the films grown on the substrates with large paramagnetic behavior, for example, NGO. Figure 3-8 shows the magnetization of the film

$(\text{La}_{0.4}\text{Pr}_{0.6})_{0.67}\text{MnO}_3$ grown on NGO. The paramagnetic signal is clear visible on the upper panel of the figure. The lower panel shows the M - H loop of the film which shows that the sample is around 67% ferromagnetic. The fully ferromagnetic sample of this type would show a magnetization of $3.67 \mu_{\text{B}}$ per Mn site.

Table 3-1 : Lattice mismatch strain of the film LPCMO grown on different substrates. Note that the lattice parameter of LPCMO film is 3.84 Å.

Substrate	Crystal structure	Lattice parameters (Å)	Strain on LPCMO
NdGaO ₃ (NGO) (110)	Orthorhombic	a= 5.426 b= 5.502 c= 7.706	0.52% (tensile)
SrTiO ₃ (STO) (100)	Cubic	a=3.905	1.69 % (tensile)
LaAlO ₃ (LAO) (001)	Pseudo cubic	A=3.789	1.32 % (compressive)

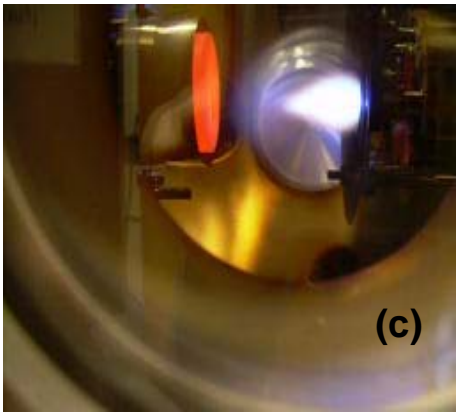
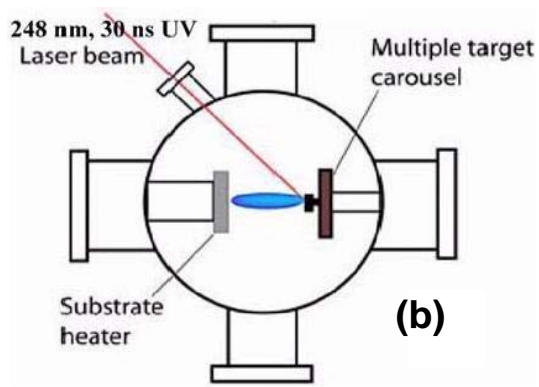
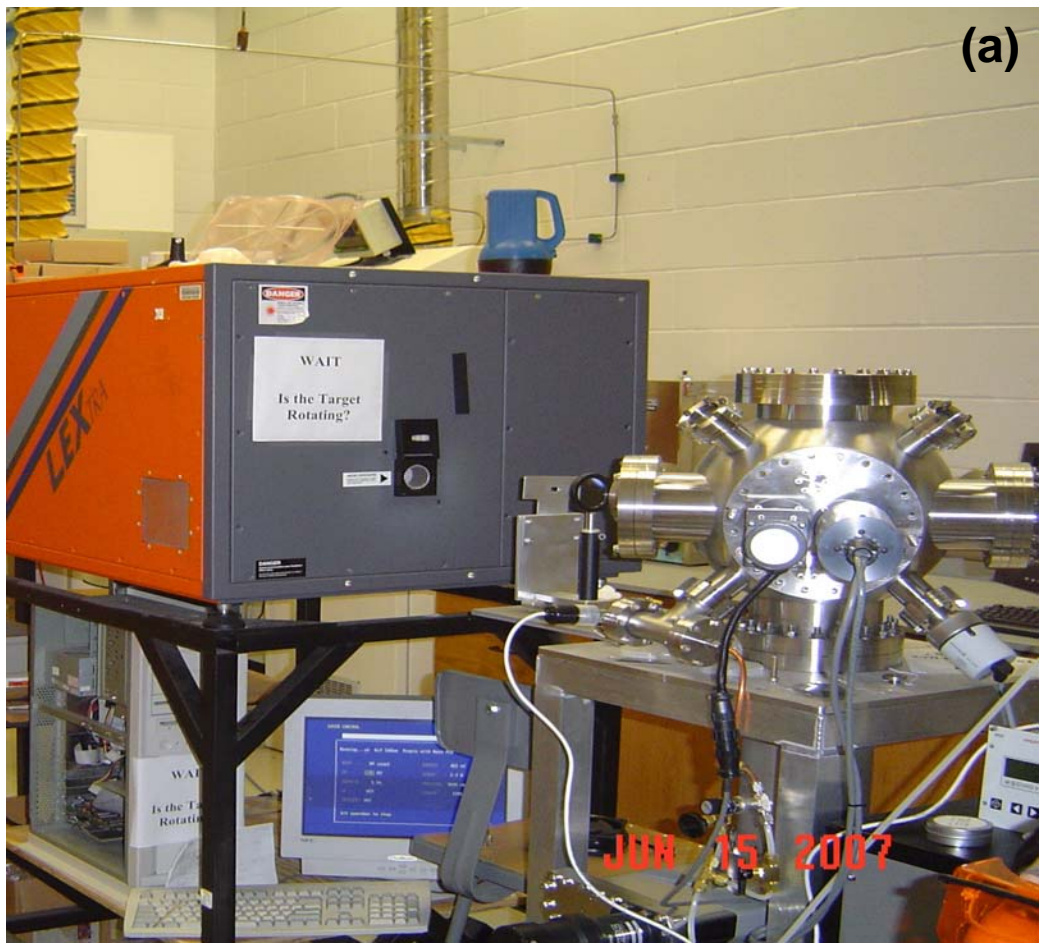


Figure 3-1: Pulsed laser deposition system. (a) LEXtra laser system and the growth chamber. (b) The schematic of the deposition technique. (c) The plum of disintegrated manganese ions and the heater glowing can be seen during a typical film growth.

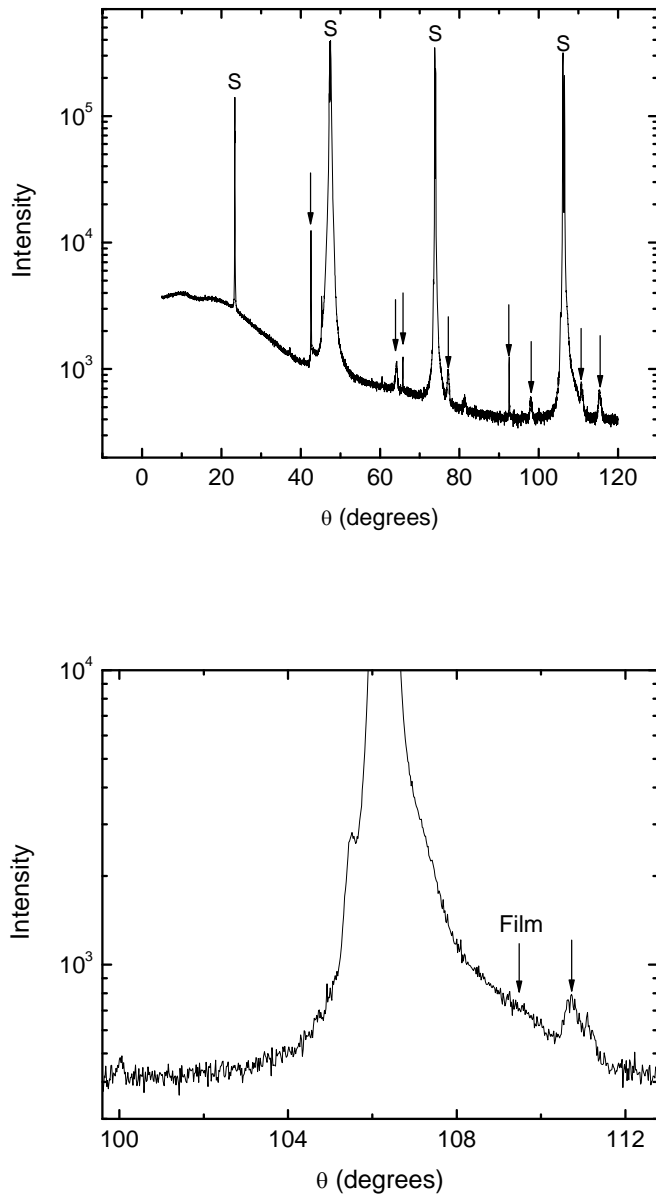


Figure 3-2: X-ray diffraction peaks of the film $(\text{La}_{0.5}\text{Pr}_{0.5})_{0.67}\text{MnO}_3$ grown on NGO substrate. The lower panel is an expanded region of the upper panel graph, which shows a shallow peak due to the film.

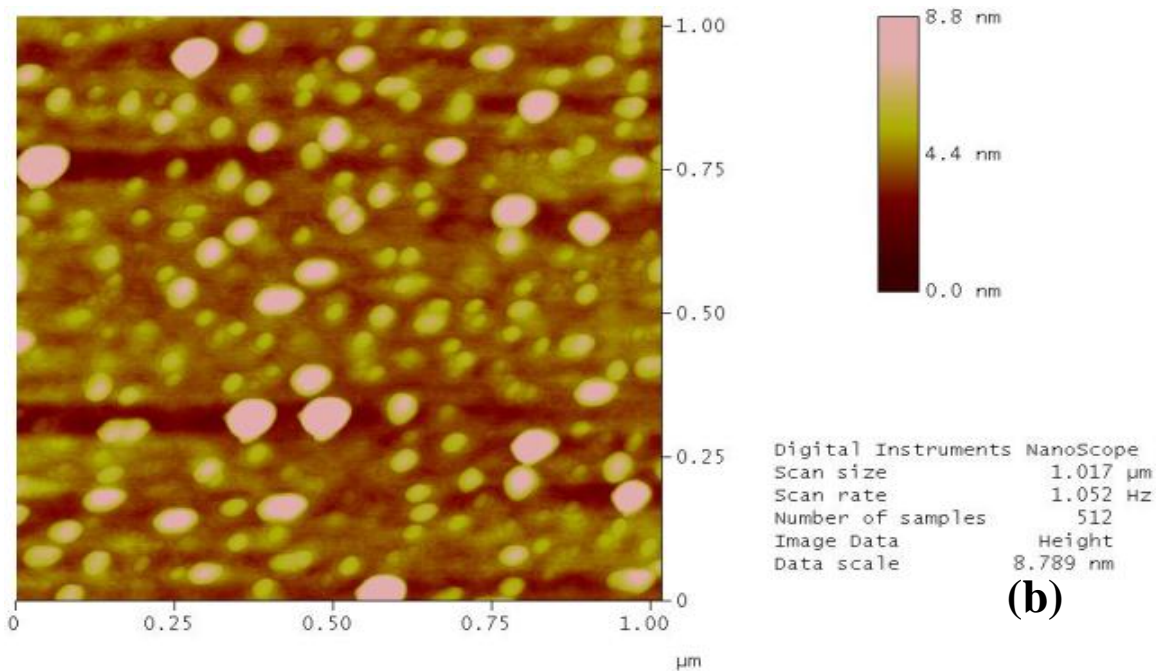
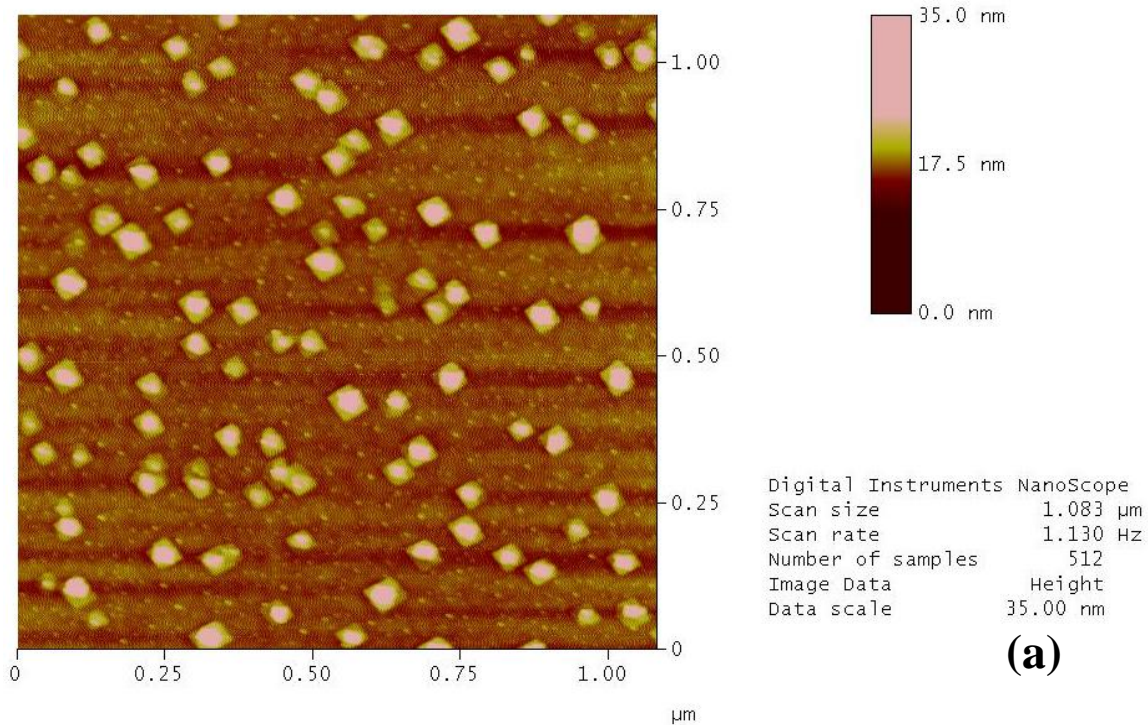


Figure 3-3: Atomic force microscopy image of $(\text{La}_{1-y}\text{Pr}_y)_{0.67}\text{Ca}_{0.33}\text{MnO}_3$ with $y=0.5$. (a) The film grown on a substrate of STO (100). Because of the large lattice mismatch, the material is grown as disconnected islands. (b) A film grown on NGO (110) substrate. Small lattice mismatch lets the manganite grow as connected islands.

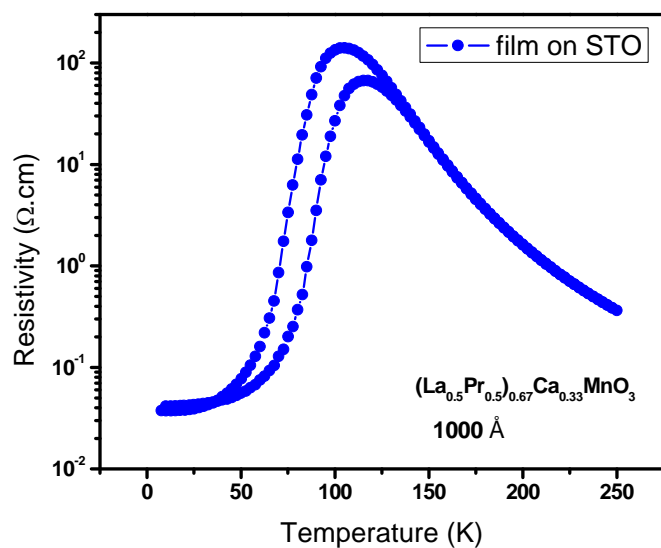
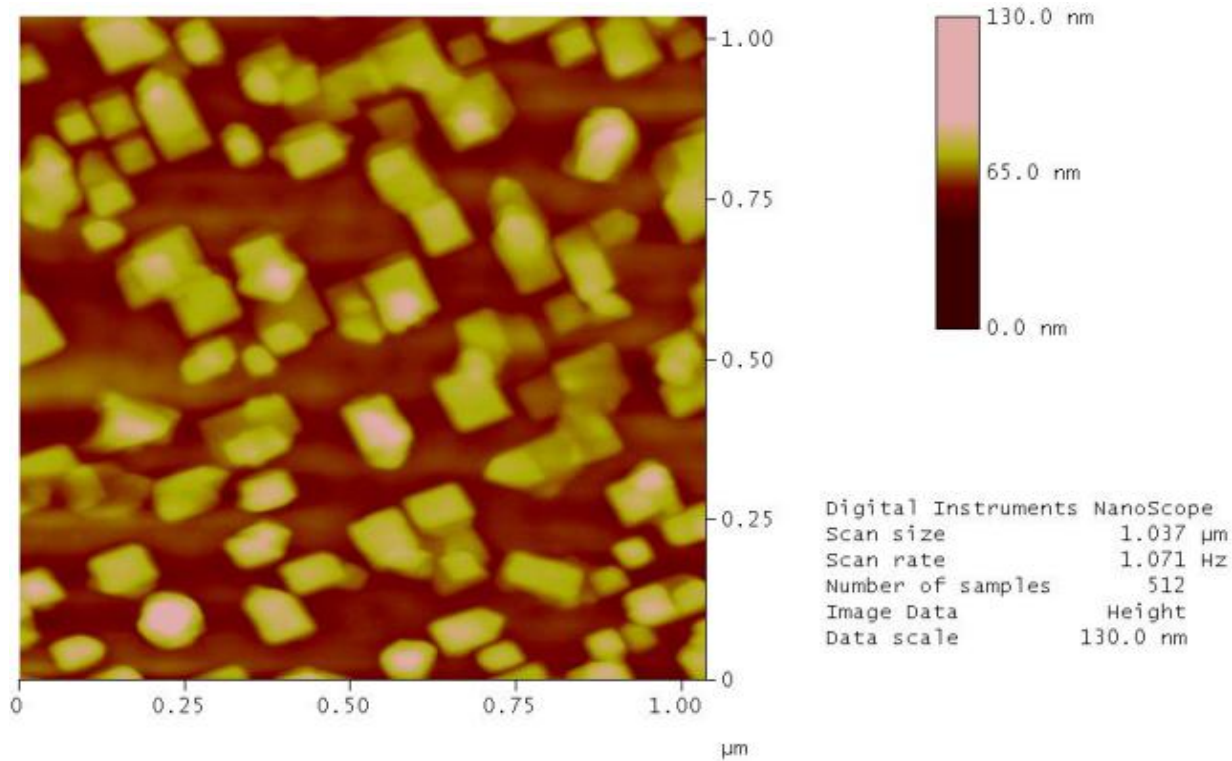


Figure 3-4: An AFM image of a 1000 Å thick film of $(\text{La}_{0.5}\text{Pr}_{0.5})_{0.67}\text{MnO}_3$, grown on STO (001) substrate. Lower panel shows the resistivity of the same film.

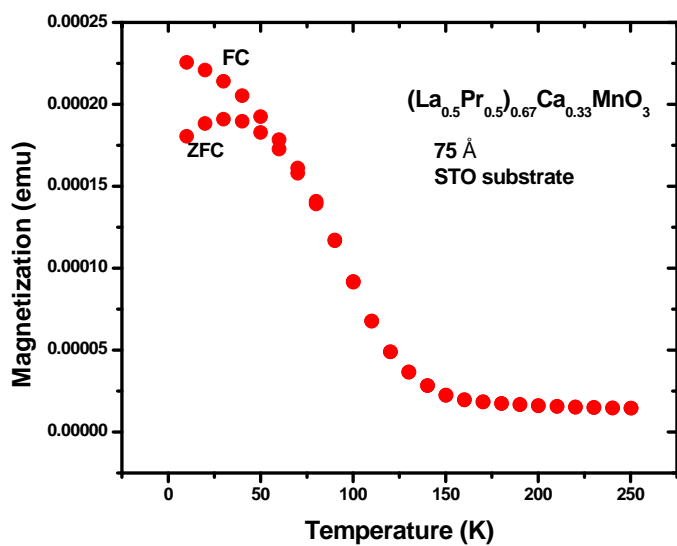


Figure 3-5: Magnetization as a function of temperature in a thinner (75 Å) strained LPCMO film grown on STO substrate.

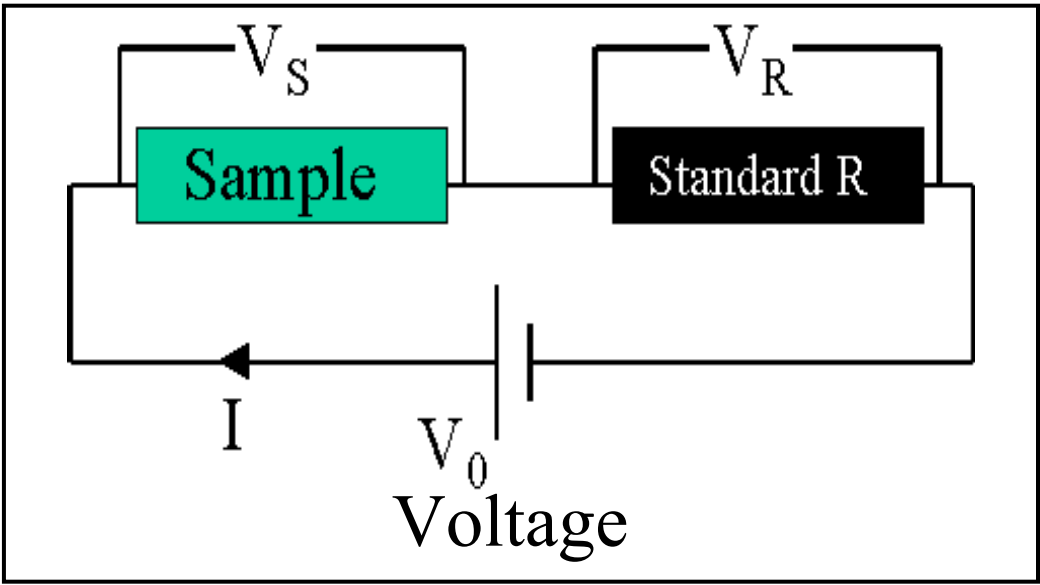
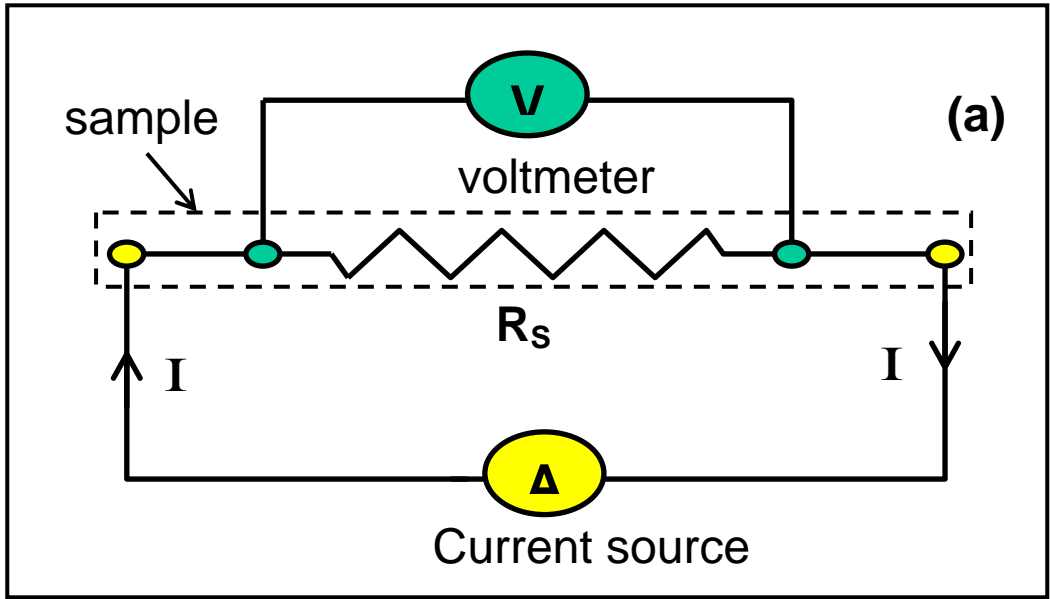


Figure 3-6: Two different methods of measuring resistivity. (a) 4-probe method. Here R_s is the sample resistance, V is the voltmeter and A is the current source. (b) 2-probe method. The standard resistance is kept at room temperature and voltage dropped across it measured by a voltmeter. Voltage source is used to supply a constant voltage (V_0).

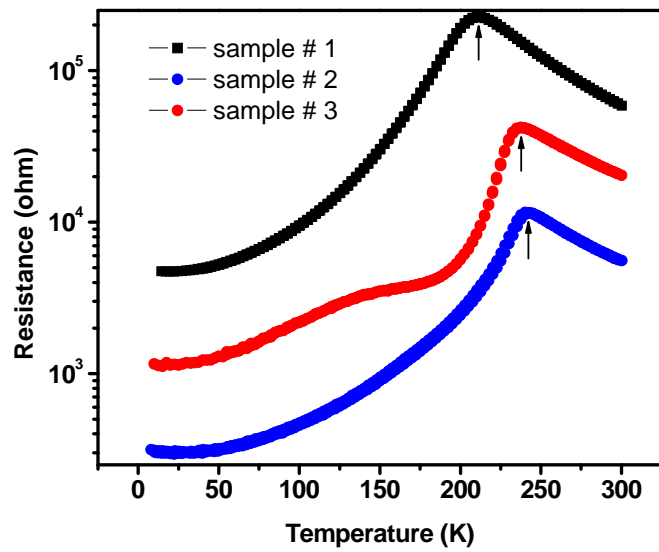


Figure 3-7: Resistance (R) as a function of temperature (T) of $\text{La}_{0.67}\text{Mn}_{0.33}\text{MnO}_3$ for various oxygen pressure.

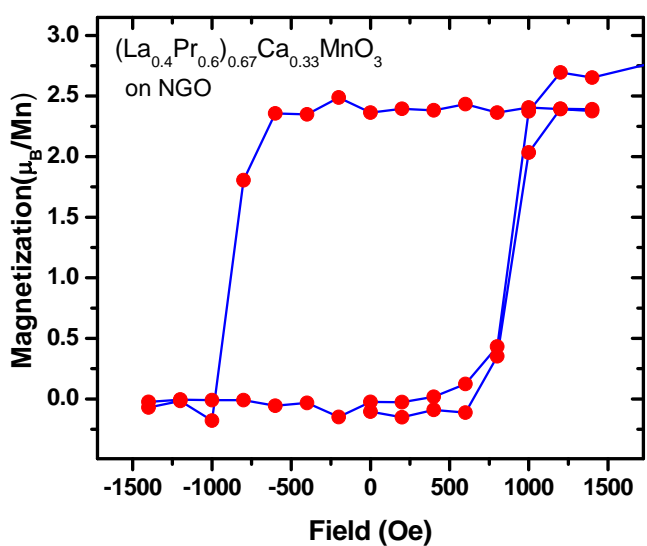
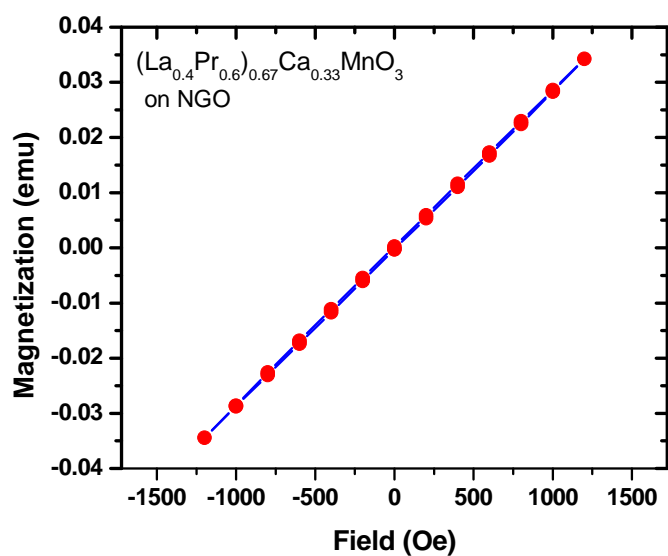


Figure 3-8: Magnetization as a function of applied magnetization in $(\text{La}_{0.4}\text{Pr}_{0.6})_{0.67}\text{MnO}_3$ grown on NGO substrate. The upper panel shows the magnetization shows linear behavior due to the large paramagnetic substrate background. The lower panel is plotted after subtracting the paramagnetic linear background.

CHAPTER 4 ELECTRIC FIELD EFFECT

We have studied the effect of substrate-induced strain on the properties of thin films of the hole-doped manganite $(\text{La}_{1-y}\text{Pr}_y)_{0.67}\text{Ca}_{0.33}\text{MnO}_3$ ($y=0.4, 0.5,$ and 0.6) grown on NdGaO_3 (NGO) substrates, in order to distinguish between the roles played by long-range strain interactions and quenched atomic disorder in forming the micrometer-scale phase separated state. We show that a fluid phase separated (FPS) state is formed at intermediate temperatures similar to the strain-liquid state in bulk compounds, which can be converted to a metallic state by applying an external electric field. In contrast to bulk compounds, at low temperatures a strain stabilized ferromagnetic metallic (FMM) state is formed in the $y=0.4$ and 0.5 samples. However, in the $y=0.6$ sample a static phase separated (SPS) state is formed similar to the strain-glass phase in bulk compounds. Our results suggest that the substrate-induced strain is a function of temperature. Hence, we show that the temperature induced variation of the long-range strain interactions plays a dominant role in determining the properties of thin films of phase-separated manganites.

Motivation

Multiphase coexistence in hole-doped manganites is a result of the competition between phases of different electronic, magnetic and structural orders, which leads to properties such as colossal negative magnetoresistance (CMR) [44, 45]. At low temperatures the two competing phases are the ferromagnetic metallic (FMM) and charge-ordered insulating (COI) phases. In manganites with greater average A -site cation radii ($\langle r_A \rangle$) and consequently a larger effective one electron bandwidth (W), the pseudo cubic FMM phase is favored at low temperatures [46]. When smaller ions such as Pr are substituted at the A -site, the pseudo tetragonal (distorted) COI phase then has a comparable free energy to the FMM phase, resulting in micrometer scale phase

separation [6]. It was shown that in the presence of quenched disorder introduced by the ions of different radii, the similarity of the free energies leads to coexistence of the two competing phases [45]. However, the observation of martensitic strain accommodation in manganites [47] and fluid like growth of the FMM phase observed in magnetic force microscopy (MFM) images of phase separated manganites [5] suggest that the phases are not pinned, which can be explained by an alternative model which shows that phase separation occurs due to the different crystal structures of the FMM and COI phases and the resultant long range strain interactions [44]. In fact, due to this behavior the phase separated state in manganites has been described as an “electronic soft matter” state [45, 48], which are similar to the phases observed in the materials such as liquid crystal [49]. To understand the underlying mechanism for micrometer scale phase separation in manganites and propose possible technical applications, it is essential to distinguish between the roles played by quenched disorder and long range strain interactions.

If long range strain interactions are the principal cause of phase coexistence, then it should be possible to control the elastic energy landscape with substrate induced strain. Strain-induced phase separation has been clearly observed in thin films of $\text{La}_{0.7}\text{Sr}_{0.3}\text{MnO}_3$ grown using laser molecular beam epitaxy [50] and substrate strain is known to affect the nature of structural transitions in ferroelectrics [51]. On the other hand, the effect of quenched disorder can be estimated from the effect of isovalent substitution of La-ions by the smaller Pr-ions. In this chapter we report our results on the separate effects of substrate induced strain and isovalent substitution in thin films of the manganite $(\text{La}_{1-y}\text{Pr}_y)_{0.67}\text{Ca}_{0.33}\text{MnO}_3$ (LPCMO), and compare our results to bulk LPCMO. The T - H phase diagram of bulk LPCMO clearly shows two distinct types of phase separation (PS), a strain-liquid (dynamic PS) and a strain-glass (frozen PS) regions [52]. We show that in thin films of LPCMO, a fluid phase separated (FPS) state is

formed at intermediate temperatures similar to the strain-liquid state in bulk materials. However, a strain stabilized FMM phase is formed at low temperatures leading to a sharper and larger drop in resistivity compared to bulk samples. The strain stabilized FMM phase transforms to a static phase separated (SPS) state (analogous to the strain-glass state in bulk LPCMO when the Pr content is increased. The FPS and SPS states were named based on the fluid like and static behavior of the FMM regions in the temperature range of the FPS and SPS states, respectively, as observed in MFM images of LPCMO [5]. Corresponding to our nomenclature of the phase separated states we show that an external electric field transforms the FPS state to a metallic state whereas there is negligible electric field effect once the sample reaches the SPS state.

Experimental Details

We have grown thin films of $(La_{1-y}Pr_y)_{0.67}Ca_{0.33}MnO_3$ (LPCMO) ($y=0.4, 0.5, \text{ and } 0.6$) using pulsed laser deposition (PLD). The films were grown in an oxygen atmosphere of 450 mTorr on $NdGaO_3$ (NGO) (110) and $SrTiO_3$ (STO) (100) substrates kept at 820 °C. All the films described here are 30 nm thick and were grown at a rate of about 0.05 nm/s. These growth conditions were optimized to obtain an insulator-to-metal transition temperature while cooling T_{IM} (cooling) close to that observed in bulk compounds of similar composition and the minimum transition width at T_{IM} (cooling). Such an optimization is crucial for mapping the phase diagram of LPCMO, since the properties of thin films of this compound vary markedly depending on the growth conditions. Standard $\theta-2\theta$ x-ray diffraction data show that the films are epitaxial and of a single chemical phase. Since the resistance of the films can be as high as 1 G Ω , the resistivity ρ , of the films was measured with a two-probe method using a constant voltage source, as shown in the lower inset of figure 4-1, with V_0 set at 5 V. We measured the voltage V_R across the standard resistor R . The current in the circuit then was V_R/R and the voltage across the sample $V_S=V_0-V_R$. Hence, the sample resistance $R_S = (V_0-V_R) \times R/V_R$. As a check, the low temperature resistivity was

also measured using a standard four-probe method. The I - V curves to be shown later were measured by varying V_0 . For the ρ vs. T curves, the temperature was varied at a rate of 2 K/min.

Results and Observations

Hysteresis in Resistivity

The ρ vs. T data for three LPCMO films grown on NGO ($y=0.4, 0.5,$ and 0.6) and one LPCMO film grown on STO ($y=0.5$) are shown in figure 4-1. An expected reduction of T_{IM} (cooling) is observed with increasing Pr concentration due to the reduction of $\langle r_A \rangle$. The width of the hysteresis between warming and cooling cycles of temperature drops sharply when y is reduced from 0.5 to 0.4 (Fig. 4-1, top inset). A remarkable feature of the resistivity is that, unlike in bulk $(La_{1-y}Pr_y)_{0.67}Ca_{0.33}MnO_3$ (LPCMO) [6], the residual resistivity ρ_0 (measured at 10 K) does not change from $y=0$ ($La_{0.67}Ca_{0.33}MnO_3$, LCMO) to $y=0.5$ and then rises sharply for $y=0.6$ (Fig. 4-1, top inset).

Phase Diagram

We mapped the T - H phase diagram of the $y=0.6$ sample by measuring resistance R vs. H curves at different temperatures for the cooling cycle (Figs. 4-2 right panel). Since the effect of H is irreversible, the sample was reset after every field sweep by heating it to 150 K and then cooling it to the set temperature. The data points were obtained by locating the magnetic field corresponding to the steepest change in R at a given temperature, i.e., where dR/dH is maximum (Fig. 4-2 right panel). The squares and triangles represent the melting and freezing fields, respectively (Fig. 4-2, left panel). The melting field line is extended to zero field by including the T_{IM} (cooling) at zero field from figure 4-1. The inverted triangles represent the melting field at low temperature ($T \leq 50$ K). Since the transition widths can be large in thin films (Fig. 4-2, right panel), as shown by the error bars in the left panel of Fig. 4-2, we have used a more direct

method of constructing the T - H phase diagram. We plotted the difference in $\log(R)$ between up sweep and down sweep of H , $\log(R_{up}) - \log(R_{down})$, in the T - H plane as a 2D color plot (Fig. 4-2, left panel).

The two methods of plotting the phase diagram give similar results except that the SPS region can be clearly distinguished only with the second method. Four distinct regions can be clearly identified in this phase diagram. Two pure phases namely the COI state and the FMM state and two mixed phase states, namely, the fluid phase separated (FPS) state and the static phase separated (SPS). As mentioned earlier, the nomenclature of the mixed phase states is based on the electric field effect (explained in the later sections) and the previously reported MFM images of LPCMO thin films [5].

Nature of Phase Coexistence

To elucidate the nature of phase coexistence in our thin films of LPCMO, we have to understand the combined effect of substrate induced strain and Pr substitution. NGO (110) has an orthorhombic structure with two in-plane distances of 3.853 and 3.861 Å at room temperature, which stabilizes the pseudo cubic structure with negligible strain when manganites such as LCMO are grown on NGO [36, 9]. Hence the substrate tends to stabilize the pseudo cubic FMM phase at low temperatures in LPCMO samples grown on NGO (110) substrates. Conversely, Pr has a smaller cation radius than La and hence, substitution of La ions by Pr ions favors a distorted crystal structure [53]. The distortion produced by Pr substitution reduces the T_{IM} (cooling) in our LPCMO thin films similar to bulk LPCMO [6]. On the other hand, strain induced by the NGO substrate removes the resistivity anomaly at the charge-ordering temperature (T_{CO}) seen in bulk LPCMO [6], which is an effect of the suppression of the bulk structural transition near T_{CO} [54]. Therefore, although the films are under negligible substrate strain at room temperature, the structural phase separation of the bulk material as the temperature

is lowered [6] results in a strain build up in the thin film. A similar effect has been shown for ferroelectric thin films where the strain in the film is released by the formation of domains with different structures aided by the defects in the film [55]. A similar structural separation in manganites would lead to phase separation into FMM and COI regions and the observed reduction of T_{IM} (cooling). Furthermore, the thermal contraction of the substrate modifies the strain landscape leading to the fluid nature of the phases as has been observed in MFM images of LPCMO thin films [5]. A detailed temperature dependent structural study of the thin films is required to verify the above hypothesis. However, it is clear from figures 4-1 and 4-2 that in spite of substrate induced strain, the phase diagram of the LPCMO ($y=0.6$) sample is similar to that of bulk LPCMO [52].

In contrast to the $y=0.6$ sample, ρ_0 for the $y = 0.4$ and 0.5 samples drops to a value consistent with the pure FMM phase of the $y=0$ sample (Fig. 4-1, upper inset). Magnetization measurements also show that the $y=0.5$ sample has a saturation magnetization (M_{sat}) consistent with a pure FMM phase. M_{sat} is estimated by measuring the $M-H$ loops for the thin films and then subtracting the paramagnetic background due to the NGO substrate. Hence, these two samples have a pure FMM phase at low temperatures in contrast to the strain-glass phase observed in bulk LPCMO [52], because the NGO substrate favors the pseudo cubic FMM phase at low temperatures. When the Pr concentration is increased to $y=0.6$, ρ_0 increases by about an order of magnitude to $8.7 \text{ m}\Omega\text{-cm}$. The value of M_{sat} for this sample is consistent with 67 % of the material being in the FMM phase at low temperatures (lower panel of the figure 3-6) . As shown in the left panel of Fig. 4-2, a phase similar to the strain glass phase in bulk LPCMO (the SPS state) appears in the phase diagram of thin film LPCMO only when the Pr concentration is increased to $y=0.6$. It was suggested in Ref. [52] that the strain-liquid to strain-glass transition is

due to the interaction of the long-range strain with the quenched atomic disorder. The observation of the FPS state and the absence of the SPS state in the $y=0.5$ sample show that under substrate induced strain, long-range strain is the driving force behind micrometer scale phase separation in manganites. Figure 4-1 also shows the resistivity of a $y=0.5$ film on an STO (100) substrate (STO has a cubic structure with a lattice constant of 3.905 \AA which translates to a biaxial tensile strain of 1.2% for a thin film of a manganite such as LCMO grown on STO. The film was insulating down to the lowest temperature of 5 K (data not shown down to 5 K due to high resistance values) which suggests a large strain effect. However, atomic force microscope images revealed different growth modes for the films on NGO and STO which makes it impossible to quantify the change in the strain on these two different substrates since it is known that different growth modes lead to different local strain distributions [36, 9].

Nonlinear Current to Voltage Characteristics

To realize potential applications, an accessible handle is needed to manipulate the phase separation in these thin films and one candidate is an external electric field. Previous measurements of the electric field effect showed a large drop in the resistivity of charge-ordered manganites on the application of an electric field [7]. Electric field effects have also been observed in thin films of LPCMO [56]. Large electric current effects have been observed in LPCMO crystals due to Joule heating of the metallic regions [57]. In our samples, the voltage was applied to the LPCMO thin films using two indium contacts 0.75 mm apart. The circuit for measuring the I - V curves is the same as the one used for measuring resistivity. Figure 4-3 shows the I - V curves for the $y=0.6$ sample for the cooling run. At a threshold voltage V_{th} , the current across the film rises abruptly. This electric field effect is irreversible as shown for the 59 K curve (red) in Fig.4-3. The sample stays in the low resistance state even when the electric field is

removed. To recover the high resistance state we heat the film to a temperature above the resistivity hysteresis region and then cool it down to the next desired temperature. We have plotted the quantity $\log(dI/dV)$ calculated from these I - V curves as a function of temperature and voltage to construct a T - V phase diagram as shown in Fig. 4-4 a. The observed electric field effect is not a heating effect as reported by Tokunaga *et al.* [57] since heating should increase the resistance in the temperature range shown in Fig. 4-3. We also observed a similar electric field effect while cooling the $y=0.5$ sample. Using an extended double exchange Hamiltonian, Gu *et al.* showed that the application of an electric field favors the FMM phase over the COI phase [58]. The authors also showed that V_{th} decreases as the number of high resistance elements is decreased from a 100 to 50 % of the sample, which qualitatively agrees with the observed variation of V_{th} as a function of temperature shown in Fig. 4-4 a (decreasing temperature is analogous to decreasing number of high resistances).

A schematic picture of the phase coexistence in LPCMO for the cooling cycle in the T - V plane is shown in Fig. 4-4 b. As the size of the metallic regions (shown in black) increases, the local electric field across the smaller insulating regions (shown in white) is enhanced, which leads to the predicted and observed decrease in V_{th} with decreasing temperature. Above V_{th} , percolation of the metallic regions in the film results in the sharp rise in the conductivity of the film. Further rise in the voltage across the film increases the current flowing through the metallic regions resulting in local heating and a decrease in conductivity similar to the results of ref. [57] as seen in Fig. 4-4 a (gray regions in Fig. 4-4 b). When the sample is cooled down to the SPS state, the metallic regions form a percolating path and increasing the voltage across the sample only results in a larger current and Joule heating. In contrast to the cooling run, no sharp increase

in current was observed during the warming run as shown in Fig. 4-5, which suggests that there is no enhancement of the local electric field.

This is due to the static FMM regions in the warming run [5]. The I - V behavior during cooling for a similar resistance value is shown for comparison (red curve). Therefore, once the sample is cooled to the SPS region, the FMM and COI phases are locked in space. Since the FMM regions percolate through the sample, application of a voltage leads to Joule heating of the FMM regions. On further warming the FMM regions homogeneously transform to a high temperature insulating phase with no local enhancement of the electric field.

Conclusion

In conclusion, substrate induced strain modifies the mechanism of micrometer-scale phase separation in manganites. At intermediate temperatures [$T \sim T_{IM}$ (cooling)], long range strain interactions lead to a fluid phase separated state analogous to the strain-liquid phase in bulk LPCMO [52]. However, below a critical Pr concentration ($y \leq 0.5$) the FPS state transforms to a strain stabilized FMM phase at low temperatures, unlike the strain-liquid to strain-glass transition in bulk LPCMO [52]. A static phase separated state analogous to the strain-glass phase in bulk LPCMO is observed at low temperatures only when the Pr concentration (and hence the quenched atomic disorder) is increased above a critical value ($y \geq 0.6$). An external electric field provides an effective means to modify the phase separation in manganites since it lowers the resistance of the FPS state by two orders of magnitude due to a local electric field enhancement. However, an electric field has negligible effect on the SPS state. Further experiments using low temperature MFM are needed to find the microscopic mechanism of the electric field effect. Our model shown in figure 4-4 (b), can be verified by using low temperature MFM as it can image the shape of the magnetic domains.

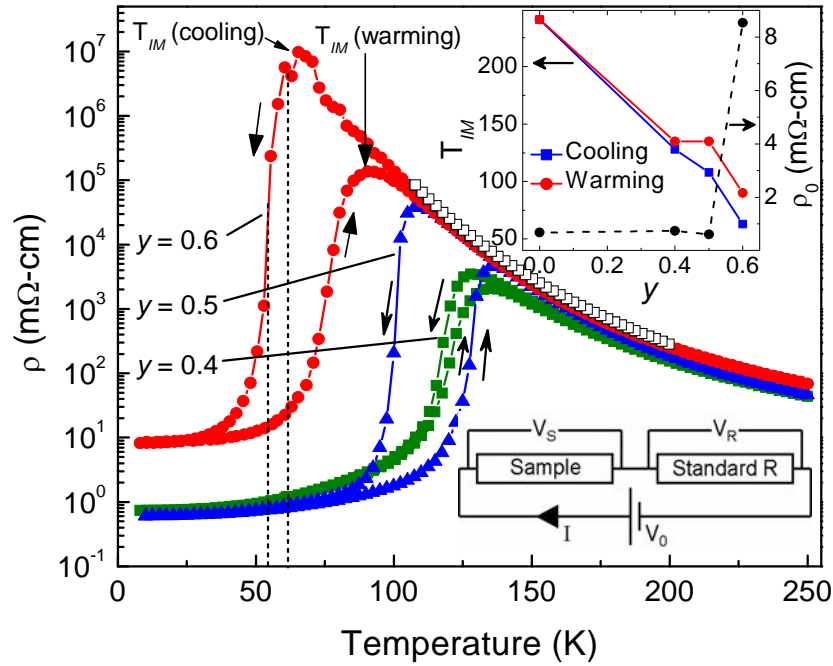


Figure 4-1: Resistivity vs. temperature curves for thin films of $(\text{La}_{1-y}\text{Pr}_y)_{0.67}\text{Ca}_{0.33}\text{MnO}_3$ ($y=0.4, 0.5, \text{ and } 0.6$) on NGO substrates. The open black squares show the resistivity behavior of an LPCMO ($y=0.5$) film on STO. Cooling and warming directions are indicated by arrows. The dotted lines mark the range of temperatures for the I - V curves shown in figure 4-2. The upper inset shows the variation of the transition temperatures and low temperature resistivity ρ_0 with y . The lower inset shows the setup for measuring the two probe resistance using a constant voltage source. All the films measured are 300 Å thick.

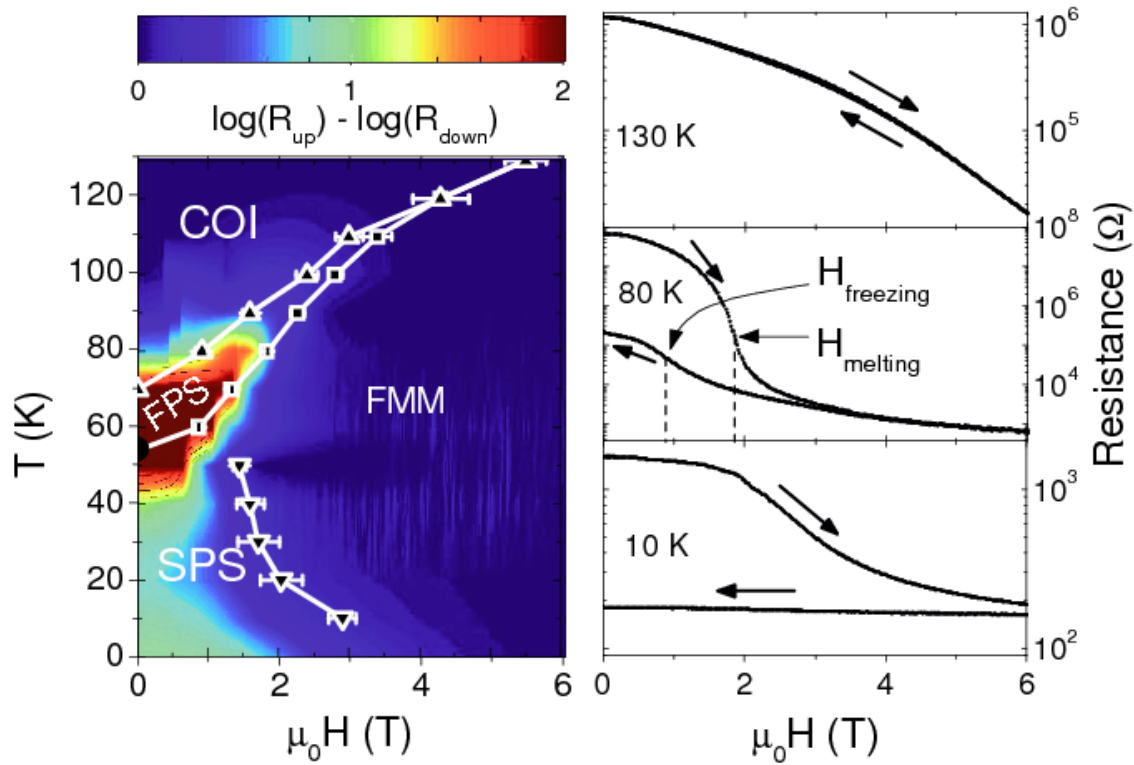


Figure 4-2: Phase diagram of LPCMO created by using R vs. H isotherms. The right panel: R vs. H isotherms for the $y=0.6$ sample in the cooling cycle for various temperature. The left panel: The T - H phase diagram for the $y=0.6$ thin film in the cooling cycle. The squares and triangles represent the melting and freezing fields, respectively. These data points were obtained by locating the magnetic field corresponding to the steepest change in R at a given temperature, i.e., where dR/dH is maximum (see right panel).

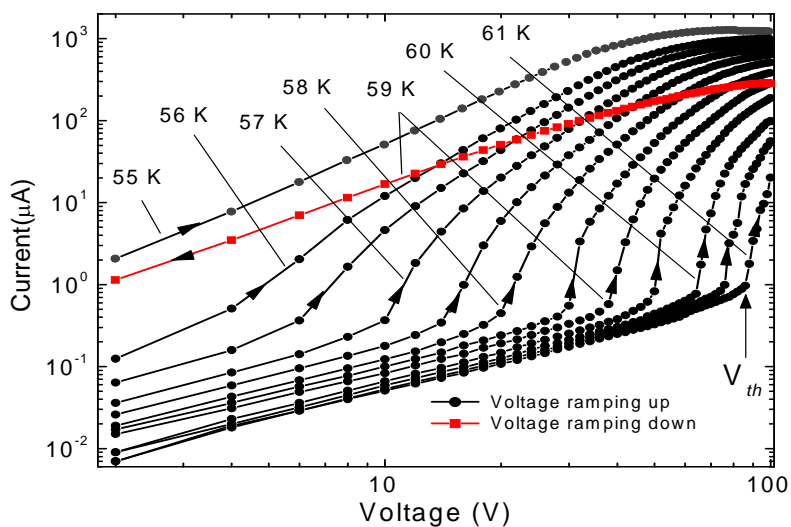


Figure 4-3: I - V curves of the $(\text{La}_{1-y}\text{Pr}_y)_{0.67}\text{Ca}_{0.33}\text{MnO}_3$ ($y=0.6$) thin film in the cooling cycle with the voltage being ramped up. The red curve is the I - V curve at 59 K with the voltage being ramped down. The irreversibility nature of the I - V curve can be seen.

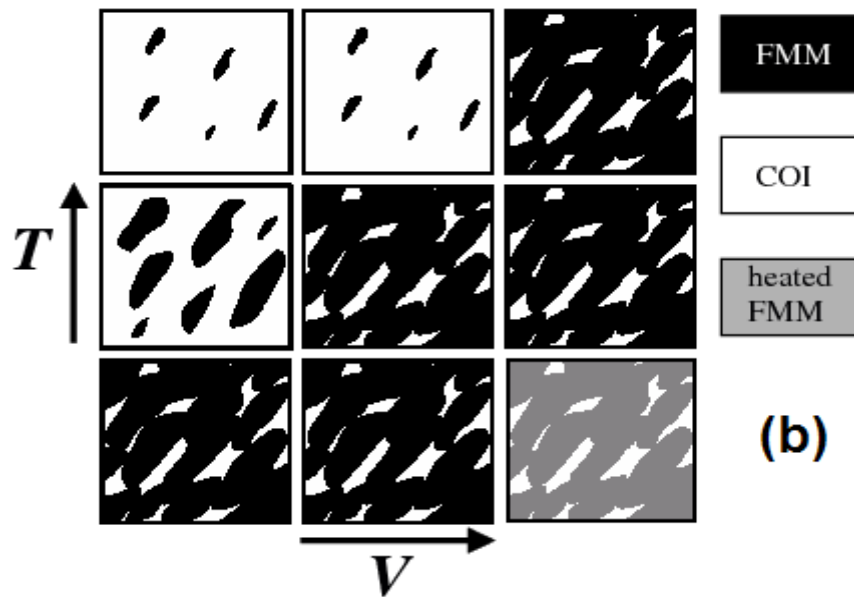
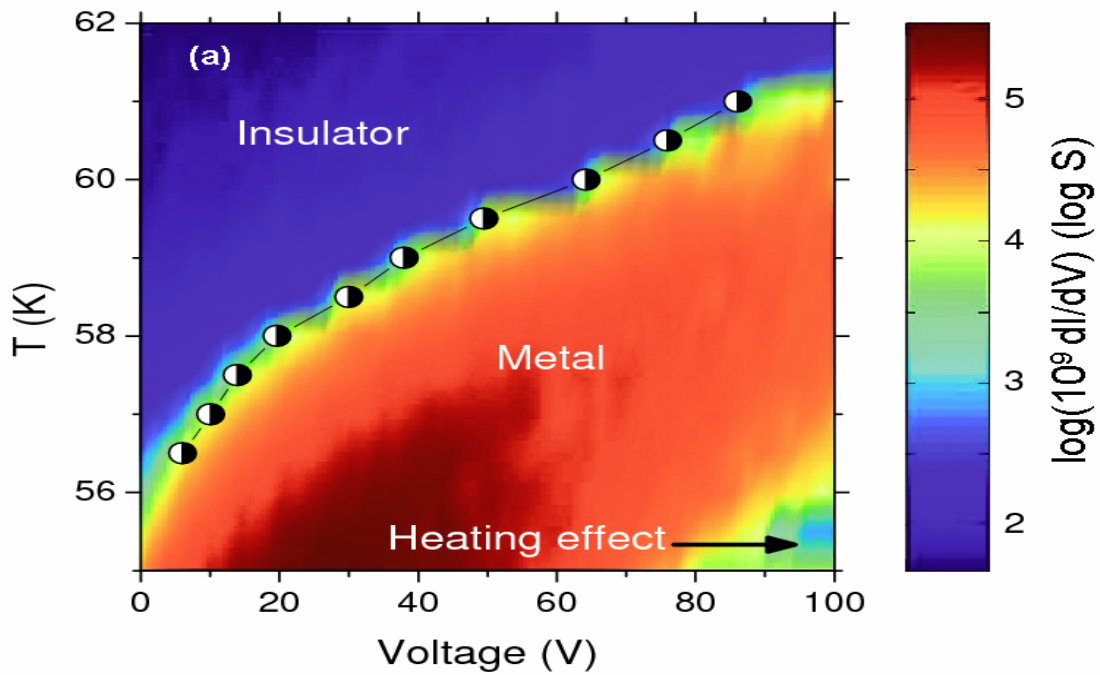


Figure 4-4: T - V phase diagram for the $(\text{La}_{0.4}\text{Pr}_{0.6})_{0.67}\text{Ca}_{0.33}\text{MnO}_3$ thin film in the cooling cycle. (a) The dI/dV is plotted as color. The black and white circles are the values of threshold voltage (V_{th}) at corresponding temperatures. This plot is overlapped on the color plot. (b) Schematic representation of the phase coexistence in the T - V plane. The black white and grey regions are FMM, COI and heated FMM respectively.

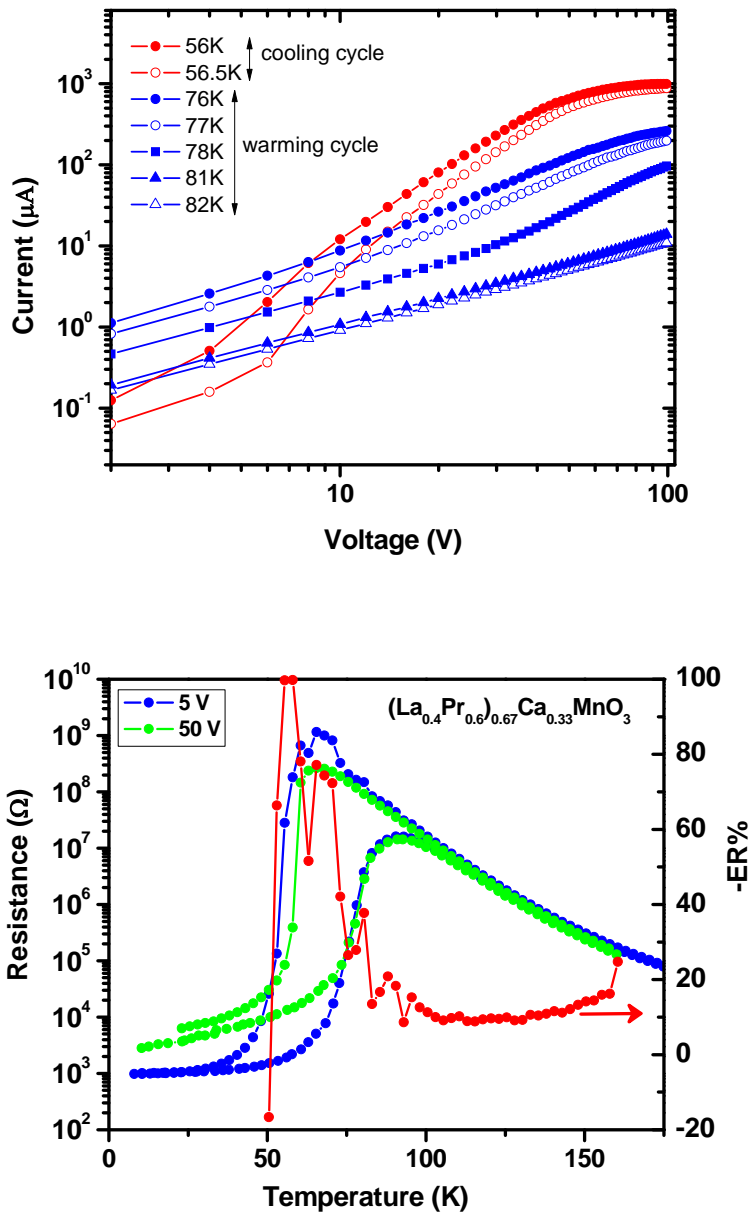


Figure 4-5: I - V curves of the $(\text{La}_{1-y}\text{Pr}_y)_{0.67}\text{Ca}_{0.33}\text{MnO}_3$ ($y=0.6$) thin film in the warming cycle with the voltage being ramped up. I - V curves (red) for the cooling cycle are shown for comparison. The lower panel shows resistance curves for two voltages. It can be seen that the resistance during cooling is largely reduced whereas the same for warming run remains the same. The negative electric resistance (electric version of CMR) calculated from these two resistances was close to 100% near peak temperatures shown by red curve on the lower panel of the graphs.

CHAPTER 5 ANISOTROPY IN TRANSPORT PROPERTIES OF MANGANITES

In the last chapter we described the effect of an electric field on a phase-separated manganite. Our experimental results which reveal the underlying mechanism of the electric field induced insulator-to-metal transition will be described here.

We have studied the dynamics of fluid like phases [52] of ferromagnetic metal (FMM) and charge ordered insulator (COI) observed in thin films of $(\text{La}_{0.4}\text{Pr}_{0.6})_{0.67}\text{Ca}_{0.33}\text{MnO}_3$ (LPCMO) under the influence of electric field. The electric field (set by applying voltage difference across the material) alters the fluid phases in a way to make the material more metallic [59]. To check if the enhanced metallicity is associated with the increase in the size of the FMM domains, we measured magnetization using SQUID magnetometer with and without electric field. The saturation magnetization remains same in either case showing that the FMM domains do not increase in size. This led us to hypothesize that the domains stretch themselves out along the direction of electric field to give rise to the abrupt percolation. This assumption was verified by measuring the transverse resistance while a voltage difference was applied longitudinally across the material. For this a cross bar (each bar 10 μm wide and 40 μm long) of manganite was fabricated by using photolithography and wet etching. At a threshold voltage when one leg of the cross bar went through percolation showing a sharp increase in current, the resistance across the other leg of the cross bar increased. This increase in resistance is thus attributed to the FMM domains being stretched in the direction of the electric field.

Motivation

The LPCMO manganites have shown hysteresis in resistivity between warming and cooling cycle and the transition from insulator to metal has been very sharp in particular during the cooling cycle. This behavior reveals the phase separation in these materials and the first order

nature of the phase transitions. The phase diagram of this material as shown in figure 4-2 of chapter 4 shows four distinct regions. There are two pure phases called ferromagnetic metal (FMM) and charge ordered insulator (COI). The remaining two phases are called fluid phase separated state (FPS) and static phase separated state (SPS). We have also called the FPS state an *electronic soft matter* like state. We have seen a strong electric field effect when the LPCMO manganites are in FPS state [59]. A voltage difference across the sample is applied to see the effect of electric field. Figure 5-1 shows the current vs. voltage characteristics of LPCMO at a temperature of 50K which is well within the FPS regime. It is clearly seen that current increases sharply as the voltage applied is above the threshold voltage (V_{th}). Once the applied voltage is above the threshold voltage, the current vs. voltage behavior is ohmic for a while. However as the voltage is increased further the current vs. voltage flattens out because of the Joule heating of the metallic filaments [57]. In addition once the sample reaches a low resistance state it continues to remain in the low resistance state even if the voltage is ramped down. Now we wanted to find out what happens to the local phases when the current through the sample sharply increases above the threshold voltage.

Experimental Results and Discussion

Magnetization as a Function of Electric Field

The increase in current due to the application of electric field can be interpreted as increased metallicity. As we know metallicity in manganites is associated with ferromagnetism. So the obvious question would be, is the increase in current due to the increase in the size of the ferromagnetic domains? To answer this question we have measured the magnetization in the material as a function of electric field. For this purpose a 5mm \times 5mm thin film of LPCMO grown on NGO (110) of thickness 300 Å was used. Two thin gold wires were soldered along the two opposite sides of the sample for the purpose of applying voltage difference between them.

Magnetization as a function of external magnetic field (M - H loop) was measured for three different conditions using a SQUID magnetometer (figure 5-2). The first one was measured without the electric field. The second one was measured by applying 40 V which is above the threshold voltage (20 V) of this material. However the measurement was done after ramping the voltage down to zero. The last one was done keeping the sample at 40 V for the duration of the measurement. The saturation magnetization in these three different cases did not show any appreciable difference as shown in figure 5-2. However the coercive field in case of the voltage being applied during the whole time of the measurement is decreased. This could have been due to the domain movement caused by the Joule heating as the voltage is applied for considerably long time when the sample is predominantly in the metallic state. The M - H isotherms overlapping on top of each other surely rules out the possibility of the ferromagnetic domains' size increase by the application of electric field.

There could be two possibilities that cause the sudden rise in current as the voltage increased above the threshold limit. One maybe that the ferromagnetic and hence metallic domains stretch in the direction of applied electric field. As we know that when a metallic conductor is exposed to an otherwise uniform electric field, the positive and negative charges will separate to two opposite directions [60]. For the sake of simplicity, if we assume the metallic domains coexisting in the matrix of charge ordered insulator as spherical, the charge distribution would be in two opposite ends as shown in figure 5-3 a. As a matter of fact there are some calculations done on the basis of effective medium approximation which shows that the metallic domains are in fact spherical [61]. The electric field in the region between the metallic regions is very high because of the smaller size of the domains. The size of these domains is in the order of hundred to thousand nanometers which gives electric field as high as 10^7 V/m. When such a high

electric field is set up between these metallic domains, which are fluid like in nature (see the phase diagram in chapter 4), they could elongate in the direction of the field. Another possibility is a metallic filament connecting the ferromagnetic metallic domains. These filaments are created by dielectric breakdown of the insulating regions in favor of metallic regions [62]. The formation of such filamentary connected path was previously suggested by Garbarino et al [63] and Wu et al [64] in single crystals of $\text{La}_{5/8-y}\text{Pr}_y\text{Ca}_{3/8}\text{MnO}_3$ ($y \sim 0.4$). The schematic of this type of filamentary connection is shown in figure 5-3 b.

Nanofabrication of a Cross Structure

We would like to distinguish between these two possibilities mentioned in the previous subsection. For this purpose we had to make a cross structure of LPCMO as shown in the upper right corner of figure 5-4. The thickness of the film is 300 Å and the dimensions of each bar of the cross are 10 µm wide and 40 µm long. If our first assumption that the metallic domains stretch in the direction of applied electric field, then the resistance along the sample in this direction should decrease. Because of this elongation along the direction of E-field, the sample gets deprived of the metallic region in the transverse direction which would increase the resistance in this direction although slightly. To be able to measure this slight increase of resistance in the direction perpendicular to the applied electric field, we had to make the cross like structure. This way we could apply voltage across one leg of the cross but would not affect the metallic regions of another leg except the ones at the center square of the cross.

The cross bar (each bar 10 µm wide and 40µm long) of our LPCMO manganite was fabricated by using photolithography and wet etching. Karl Suss MA6 Mask Aligner was used for patterning the manganite sample with UV light of wavelength 348 nm. After the fabrication, we measured the resistance of each bar to make sure that the transitions are as good as that of the bulk sample. The resistance vs. temperature graph is shown in the figure 5-4. The transitions are

sharp and the resistances between warming and cooling cycles for both the legs show hysteresis typical of bulk LPCMO. The resistances for both the legs match very well throughout the whole temperature except at low temperatures. The differences at low temperatures could be due to different cooling rates as it is harder to stabilize temperature at low temperatures. We did not reduce the width of the bars below 10 μ m because we wanted to retain the properties of the bulk of the material. Reducing the width further, the effect of single domain would be dominant [65]. Now we are ready to test which of our assumptions is true.

Transverse Resistance by Lock-in Amplifier

As shown in figure 5-4, we call the resistance along the leg gh longitudinal resistance (R_L). While the dc voltage is ramped up between two ends of the leg gh of the cross bar, we would measure the resistance along another leg ef of the cross bar. We call this the transverse resistance (R_T). We expect that if the electric field applied across gh elongates the metallic domains in the direction of the field, then the transverse resistance should increase. However, our initial measurements showed that voltage drop across ef , was affected by the voltage applied across gh . To remove the effect of the voltage across gh on the measurement of R_T we used an ac technique. We applied a small sinusoidal voltage of 0.1 V (rms) at 23 Hz across ef and measured R_T by using the 2 probe method explained in chapter 3. The only difference in this case is that the voltage source is replaced by an SR830 Lock in amplifier. The small voltage was used to make sure that it's not strong enough to cause the electric field effect. The ac voltage was used to remove the effect of the dc voltage (applied across gh) since the Lock-in amplifier measures only the voltage at a particular frequency. The transverse resistance was measured by using the real part of the voltage (V_{AB}) since across the test resistor the voltage and current are in phase. The schematic of the measurement circuit is shown in figure 5-5.

As we expected, the transverse resistance increased (albeit by only about 2% while R_L drops by more than 2 orders of magnitude) as the longitudinal voltage was increased above the threshold voltage (figure 5-6). For this sample geometry the threshold voltage is around 20 V. Before reaching the threshold voltage we can see in figure 5-6 that both the longitudinal and transverse resistances are not changing, which is a test of the effectiveness of our *ac* measurement set up. As the voltage reaches 20 V and beyond, the longitudinal resistance (R_L) is decreased. This happens because the metallic domains are brought closer by the elongation of their shape in the direction of applied electric field. R_L would decrease until the domains touch each other and equipotentials are redistributed. There is no further electric field induced elongation of the domains above V_{th} . However, Joule heating could still change the domain shapes. While R_L is decreasing, the resistance in the transverse direction (R_T) keeps on increasing. It should be noticed that both the longitudinal and transverse legs of the cross bar share the $10\mu\text{m}\times 10\mu\text{m}$ square at the crossing point. The domains within this shared piece of square are exposed to the dc electric field applied along gh . As the metallic domains elongate in one direction, they open up more insulating region in the transverse direction although slightly. This is the reason the transverse resistance (R_T) keeps on increasing as the metallic domains in the longitudinal direction stretch more and more. Once the voltage is high enough to completely stretch the metallic domains, there is no further change in both R_L and R_T . If the decrease in the longitudinal resistance was due to the thin filamentary connecting path, there either wouldn't be a change in the resistance in the transverse direction or it would decrease.

Conclusion

The resistance of the LPCMO manganite shows sharp transition and a wide hysteresis between the warming and cooling cycle of temperatures. This behavior is a signature of phase separation. The ferromagnetic metallic (FMM) domains in this material can be manipulated by

using electric field. The sharp increase in current as electric field is applied is due to these FMM domains being stretched in the direction of the field. In addition our measurements rules out the assumption that the sharp increase in current could be due the filamentary connecting path.

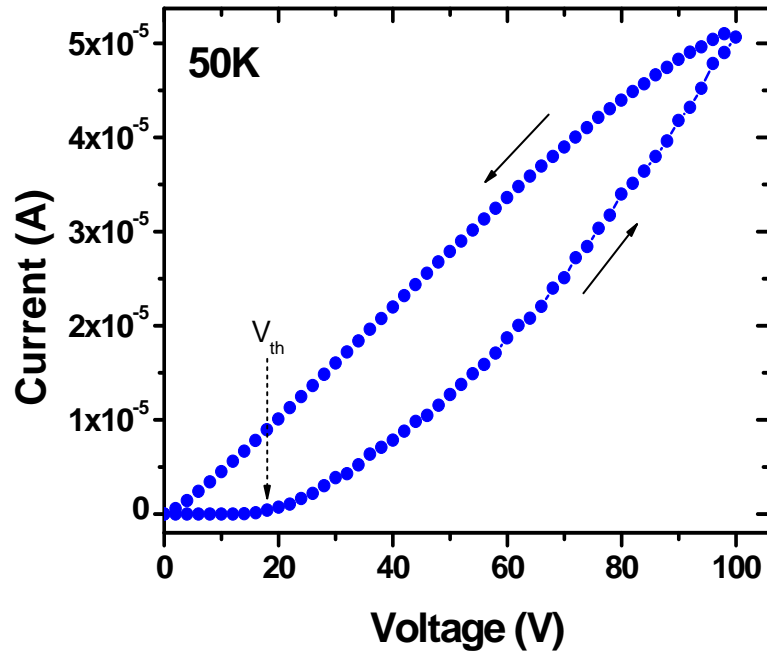


Figure 5-1: Current as a function of applied voltage in $(La_{0.4}Pr_{0.6})_{0.67}Ca_{0.33}MnO_3$. The directions of voltage applied are shown by arrows. A nonlinear increase in current is seen at a threshold voltage (V_{th}). The temperature of measurement is 50K which is in FPS state.

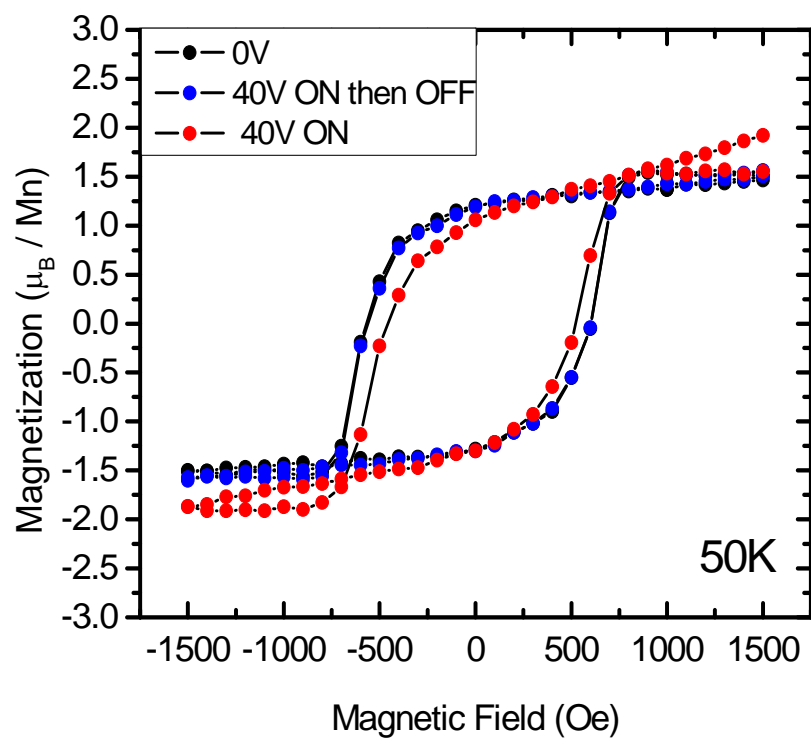


Figure 5-2: Magnetization as a function of magnetic field for three different voltages applied on $(\text{La}_{0.4}\text{Pr}_{0.6})_{0.67}\text{Ca}_{0.33}\text{MnO}_3$. This measurement was done at 50K.

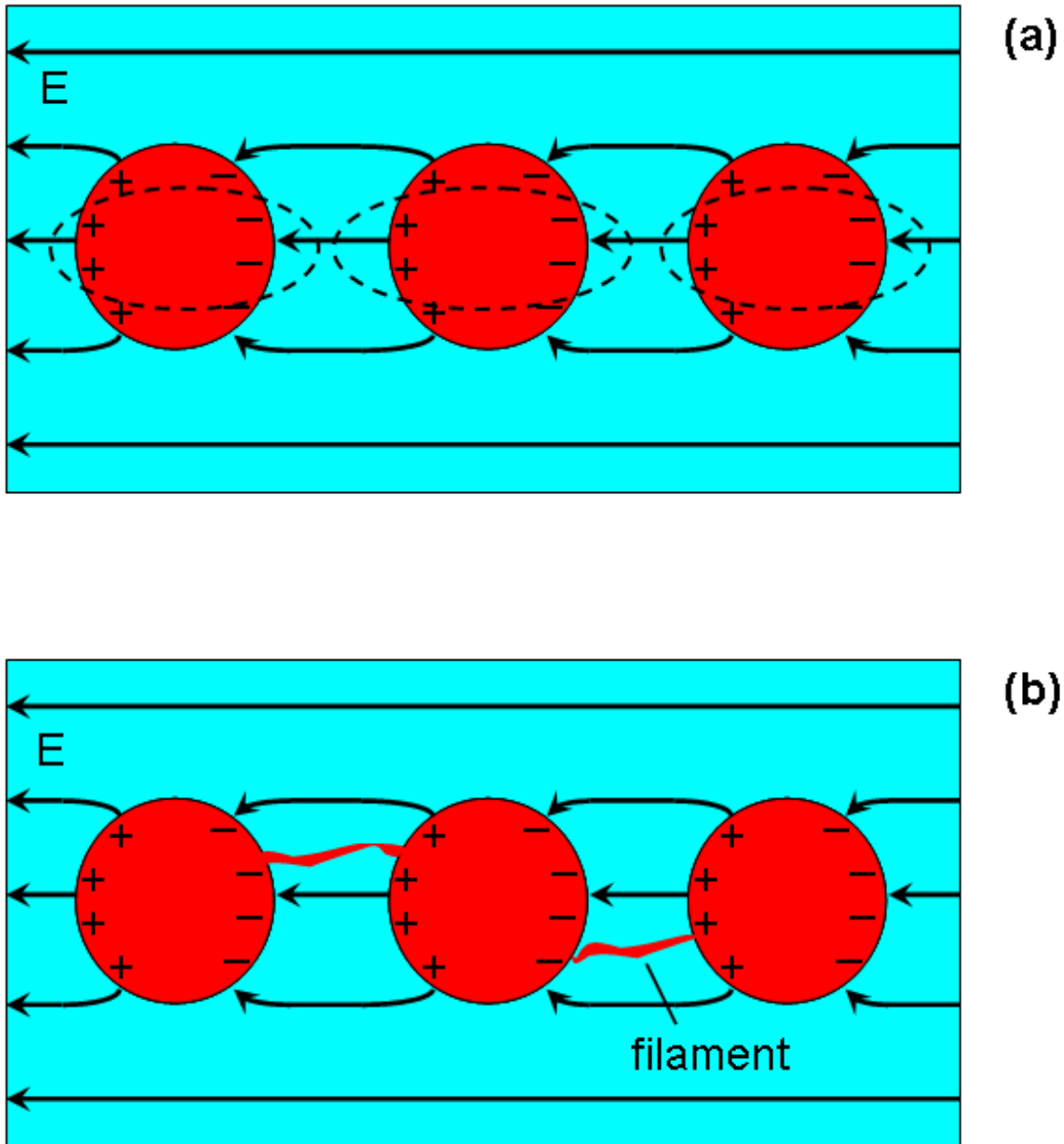


Figure 5-3: Schematic of the manipulation of metallic domains by using electric field. The red circles are ferromagnetic metallic domains and the cyan background is the charge ordered insulator. (a) The electric field elongates the metallic domains in the direction of applied field. The elongated metallic domains, which were otherwise spherical, are shown by dashed ovals. (b) The electric field creates thin metallic filaments by dielectric breakdown.

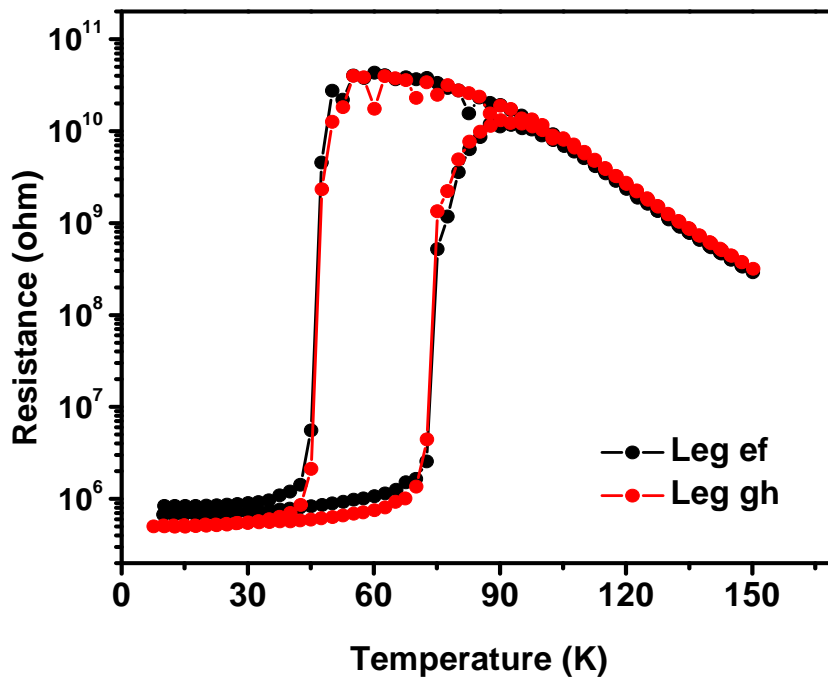
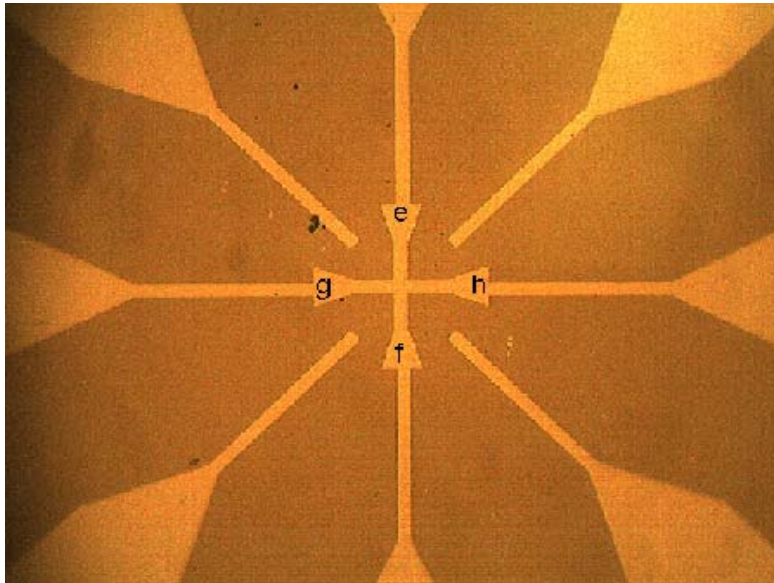


Figure 5-4: Resistance and cross bar structure. The lower panel shows the resistance of 2 legs of the LPCMO cross bar as a function of temperature. The cross bar (each bar $10\ \mu\text{m}$ wide and $40\ \mu\text{m}$ long) is shown on the upper panel of the figure.

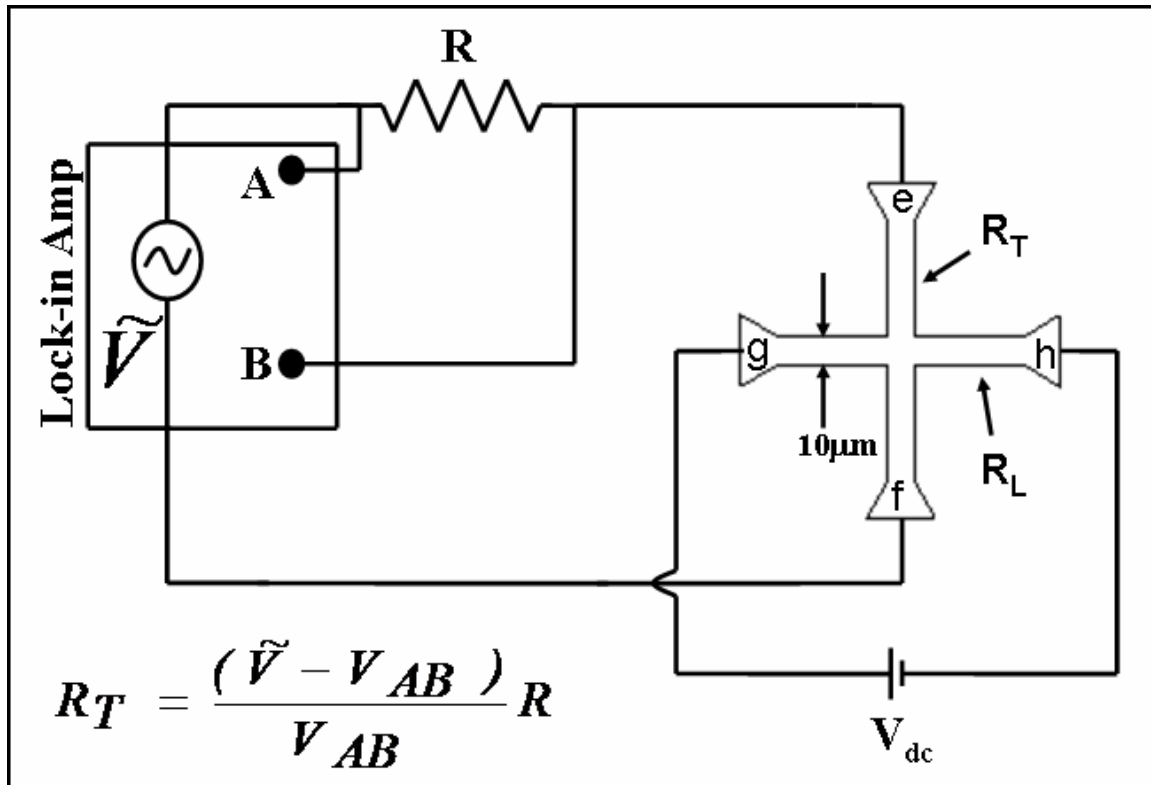


Figure 5-5: Schematic of transverse resistance (R_T) measurement while the dc voltage is being applied in longitudinal direction. The voltage across the load resistor V_{AB} is the difference between the voltages at two channels A and B.

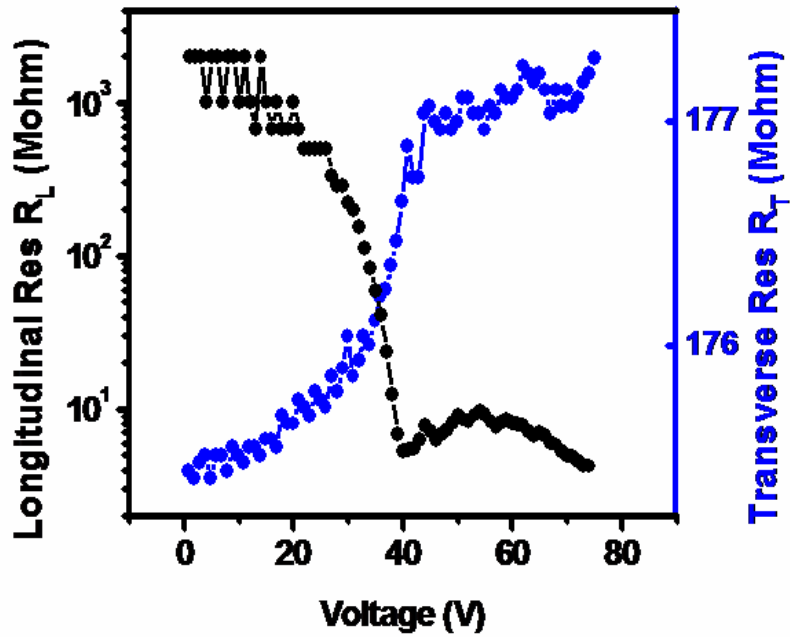


Figure 5-6: Longitudinal resistance (R_L) and the transverse resistance (R_T). The black curve is the longitudinal resistance (R_L) measured as a function of dc voltage. As the voltage is increased above the threshold voltage the longitudinal resistance decreases but the transverse resistance (R_T) (blue curve) increases.

CHAPTER 6 SCANNING TUNNELING MICROSCOPY

Motivation

In previous chapter we showed that the LPCMO exists in phase separated states. We would like to obtain conclusive evidence in support of our model for phase separation in manganites and the electric field effect. One of the tools to probe the nature of phase separation of manganites is a scanning tunneling microscope (STM) [66, 67]. We built a low temperature STM which will be used to determine the local phase of a manganite with spatial resolution of the order of 1 nanometer.

Basic Principle of Scanning tunneling Microscopy

Scanning tunneling microscopy (STM) is a tool which can take an image of a surface with atomic resolution [68-70]. The basic principle of STM is the tunneling of an electron from a tip made of a metal wire to a metallic or semiconducting surface. When the two metal electrodes (tip and the metallic surface to be scanned) are brought to a close proximity of a few angstroms, a bias voltage applied between them will cause the electron to tunnel through them. The tunneling current (I) through the junction is exponentially dependent on the junction (barrier) width (s) [71] as described by

$$I \propto \exp(-2\kappa s) \quad (6-1)$$

with the decay rate

$$\kappa = \frac{2m\varphi}{\hbar^2} \quad (6-2)$$

where φ is the effective barrier height and m is the mass of an electron.

This exponential decay of the tunnel current is a key to the imaging of a surface with nanometer scale resolution. When the metal tip is brought closer to the sample surface by a fraction of a nanometer, the tunneling current increases significantly.

Topography of Sample Surface

The exponential decay of tunnel current as the junction width increases is used to measure the height of the metal tip from the sample surface with high resolution. This height can then be converted to give the topographic image of the sample surface. As shown in figure 6-1, when the tip is scanned across the surface of the sample keeping the tunnel current constant (which is done by using a feedback system to be explained in subsequent section), we can get the surface topography by following the tip movement. The tip is made to raster scan the sample surface in x-y direction by attaching it to a piezoelectric scanner. The piezoelectric scanner is also attached to a z-voltage which is controlled by the feedback circuit to keep the sample-tip height constant.

STM Spectroscopy

The geometrical view of the atomic structure as explained in the previous section can be obtained by the dependence of current on the tip-sample position. Now keeping the tip fixed at a point close to the sample surface and measuring the current-bias voltage dependence as well as differential conductivity (dI/dV) gives us information about the local electronic structure of the material. Figure 6-2 shows the schematic of the STM spectroscopy.

The tunneling current is found to be approximately proportional to the electronic density of states as shown in the following equation:

$$I = \int_0^{eV} N_t(E)N_s(E)\tilde{t}(E)dE \quad (6-3)$$

where, $N_t(E)$, $N_s(E)$ and $\tilde{t}(E)$ are tip and sample density of states (DOS) and the barrier penetration factor respectively.

Now the derivative of the tunnel current (I) w.r.t. the bias voltage (V) is therefore proportional to the local DOS of the sample.

$$\frac{dI}{dV} \propto N_s(E)\tilde{t}(E) \quad (6-4)$$

Thus the tunneling spectra will give us the electronic state at a particular point and combining this with the topographic image, we can extract a spatial distribution of the local electronic states.

Designing Low Temperature Scanning Tunneling Microscope

The most important part for a low temperature STM head is its cylindrical macor body which contains the piezo-electric material, spring and the tip as shown in the following fig. 6-3. The STM head has to be compact so that its resonance frequencies are much higher than the frequencies of the usual sources of mechanical vibrations which are on the order of a few hundred Hz and lower. A design for such a compact STM head is described below.

The macor cylinder has a diameter of 1.5 inch (38.10 mm) and its height is 2 inch (50.80 mm). A V-shaped groove has been cut along the height of the cylinder so as to place an approach sledge. The approach sledge is also made of macor. The lower half of its body is a triangular prism like and upper half part is cylindrical. Smooth sapphire plates are attached on the 3 faces of the prism like part of the sledge. On top of the cylindrical part of the sledge, a cylindrical piezoelectric scanner is attached which is meant for swaying the tip in x-y direction and also stretch or retract in z-direction. Four shear piezo stacks are glued on the inner wall of the V-groove of the main macor cylinder, 2 on each wall. On top of each piezo stacks are attached the sapphire plates of almost the same size as the shear piezo-stacks. These sapphire plates actually provide the contact areas between the shear piezo stacks and the sapphire prism faces of the approach sledge. Once the sledge is placed on the V-groove of the macor body on top of the

shear piezo stacks, it is covered from the top by a macor plate which has remaining two shear piezo stacks attached underneath it. The macor plate is then pressed from the top by a ruby ball and a phosphor bronze spring plate. The spring plate is then screwed to the macor body to keep everything taut. The details of the design are described in the figure caption.

Approach Mechanism

The tip which is on the top of the approach sledge is first brought as close as quarter of a millimeter by a technique called *walker stepping* [72]. In this technique a snap voltage is first applied to one of the piezos, stage A as shown in figure 6-4. This snap voltage is applied such that the shear piezo stack twists backward but can't pull the sledge along with it because the sledge is held tight by other five piezos which are kept still and the voltage increase is instant. Then the snap voltages are applied to all other stacks one after another (B, C, D, E, etc.). When all the piezo stacks suffer a twist, the voltages on all the stacks are slowly decreased as shown in figure 6-4 (b). This will bring the piezo stacks slowly back to their original state and while doing this they also carry the approach sledge along with them by friction. Thus the sledge, which carries the tip and piezo scanner on its top, moves forward by a smallest distance. This process continues until the tip is very close to the sample surface. To retract the tip just opposite voltage pulses are applied to the shear piezo stacks. Caution has to be maintained not to crash the tip on the sample surface. The closeness between the sample and the tip is monitored by watching the tip movement through an optical microscope. The maximum of the voltage pulses applied on the shear piezo stacks are +/- 200 V. This set of voltage pulses can be applied at different frequency. This is used when the tip is already in a close proximity with the sample. By changing the frequency of the pulses, the tip can be brought to a tunneling range in a controlled manner. A special circuit was developed with help of the electronic shop for this purpose.

Current to Voltage Converter

The current to voltage converter circuit is shown in figure 6-5. An STM tunnel junction has a resistance of about 1 G Ω . This means that for tip-sample biases of around 1V, tunneling current through the STM junction will be around 1 nA or less (for lower biases). Because of the high impedance of the tunnel junction and the extremely small currents which have to be measured, this current has to be converted into the voltage signal and then amplified further before it is fed to the analog to digital converter (ADC) which reads the voltage signals. The current to voltage conversion and amplification is done by the current amplifier. Our current to voltage converter has two stages. The first stage has a current to voltage conversion factor of 10^7 V/A. The second stage has a voltage gain of 10 giving a total gain of 10^8 V/A. The circuit is powered by two 9V batteries which have a common ground with the signal ground. The whole circuit, including the batteries, is housed in an aluminum box. The current amplifier can be connected to either electrode of the tunnel junction (tip or sample). The input of our current to voltage converter is connected to the sample by a coaxial cable. The current to voltage converter circuit and the feedback circuit to be explained in the subsequent section were made with the help of the electronics shop of the department.

Feedback System

A feedback system is very important for imaging in a scanning tunneling microscopy. The circuit diagram used for feedback system is shown in figure 6-6. In our feedback circuit only the proportional (P) and the Integral (I) are used. The response due to a differential circuit is very abrupt, which is not good when the tip sample distance should be controlled in a nanometer scale. Since the tunneling current can be positive or negative depending on the polarity of the bias, a rectifier circuit is used to feed the modulus of the current amplifier output to the feedback circuit. This is used for carrying out bias dependent imaging. The rectified output of the current

amplifier is first compared with a reference voltage (V_{ref}) and the difference is given to the PI stage, which has two parallel gain stages, proportional (P) and integral (I), with adjustable gains. The reference voltage changes the distance between tip and the sample. The outputs of P and I gain stages are added and the sign of the output is reversed, if necessary, with a unity gain, inverting amplifier. The output of the feedback circuit is then added to the x- and y- piezo signals as explained in the summing circuit in the following section. The resultant signals are then applied to the four quadrants for x-y scanning and to keep the tip-sample height constant during topographic scans. The output of the feedback circuit can also be given to the z-piezo through a sample and hold circuit for tunneling spectroscopy. For such measurements the bias voltage is swept across a certain range while keeping the feedback in the hold mode to keep the tip sample distance constant. The sample and hold circuit is controlled by the computer. The op-amps used in the feedback circuit are OP-07, and an LF398AN was used for the sample and hold circuit. An LT1077 was used for reference circuit.

Summing Circuit

The summing circuit consists of four operational amplifiers (op-amp) as shown in figure 6-7. The output of the feedback circuit, which is the z-piezo signal is one of the inputs for all the four op-amps. The other four inputs are X^+ , X^- , Y^+ , Y^- . The X^+ and X^- are for swaying the piezo scanner in x-direction and Y^+ , and Y^- are for doing the same in y-direction. The outputs of the amplifiers $X^+ + Z$, $X^- + Z$, $Y^+ + Z$ and $Y^- + Z$ are then fed to the four quadrants of the piezo scanner. The $X^+ + Z$ and $X^- + Z$ are connected to the two directly opposite quadrants of the scanner whereas $Y^+ + Z$ and $Y^- + Z$ are connected to the remaining two opposite quadrants. By applying X or Y voltages this way, the piezo scanner can sway in x- or y- direction respectively. The resultant motion of the piezo gives a raster scan of the sample surface. Higher voltages should be applied for larger scans. The power supplies and the X's and Y's for our summing

circuit were used from the “DI ACCESS MODULE” of our commercial Nanoscope AFM from digital instruments. The inside of the scanner piezo is a non-segmented cylinder and is grounded.

Imaging Graphite

A constant current mode is used to get a topographical image of the sample surface. To get a fine atomic resolution image, we need a clean sharp tip. For this purpose a freshly cut Platinum : Rhodium (Pt : Rh ; 87:13 wt%) wire of 0.01 inch (0.25mm) diameter is used. Once the tip is inserted into the tip holder and once the coarse approach is done as explained in the previous section, the probe which is holding the STM head is first inserted into the vacuum can (figure 6-8) and then the vacuum can is put into the Dewar which has a 2.5 inch wide superconducting magnet bore. Such a wide bore magnet bore was specially ordered for our STM system from American Magnetics. The Dewar which contains our STM vacuum can is then air lifted from the ground for vibration isolation as shown in the figure 6-9. The MICRO-g vibration isolation system from Technical Manufacturing Corporation (TMC) was used. Three isolators used are rated for maximum load at an internal pressure of 80 psi. The tip is then brought closer to the sample surface by manually applying one set of voltage pulses at a time. While the tip is brought closer to the sample, a bias voltage is applied between the sample and the tip, until a tunneling current is seen.

Once a stable tunnel current is achieved, the feedback system is turned on (see the flow chart in figure 6-10). Then we apply voltages to the cylindrical scanner which has the tip on its head. The scanner piezo is made such that when all X-Y-Z electric configurations are applied, it can produce a roaster scan along the x-y direction and also can contract and stretch itself in z direction. During the scanning, the tunneling current is then fed to the current to voltage (I-V) converter circuit box. This changes the tunnel current into voltage and this voltage is then sent to the feedback circuit which it compares with the reference voltage. If the tip comes closer to a

bump on the surface, the tunnel current would rise exponentially which is then sensed by the feedback circuit after it gets converted to the voltage by I-V converter. Then to keep the tunnel current constant the feedback system would pull the tip away from the sample. On the other hand if the tip comes to a niche rather than a bump, the tunnel current would decrease. In this case the feedback system will push the tip closer to the surface by applying more z-voltage to the cylindrical scanner. This way the tip would neither crash on a bump nor move flat without noticing the niche, but would just follow the geometry of the surface with nanometer scale resolution. This movement of the tip when repeated in all x-y-z direction will give us the atomic resolution picture of the surface scanned. Figure 6-11 gives an image of graphite at room temperature. Graphite was used for calibration purposes as the inter atomic distances between the graphite atoms are already known. The piezoelectric scanner has a gain of 2 nm/V, which was found by looking at the tip scan distance at a certain voltage.

Scanning Tunneling Potentiometry

The atomic imaging and the STM spectroscopy explained in the previous sections are done in the material with metallic conductivity. Tunneling is extremely difficult in a material with high resistivity. In such a case the alternative technique called scanning tunneling potentiometry (STP) is very significant in characterizing the distribution of potential across the materials [73, 74]. The circuit diagram for this STP technique is shown in figure 6-12. As shown in figure, it has two feedback system, one for usual topography and another is for poentiometry. The sample and the tip is biased by a spatially uniform and ac voltage and a spatially varying dc voltage is applied between the two ends of the sample. The tunnel current due to the ac voltage is fed to the current to voltage amplifier which converts the current signal into a voltage signal. The voltage signal is sent to a lock-in amplifier which only lets the voltage of the same frequency as that of ac bias used between the tip and the sample pass through it. The output of the lock-in amplifier is

then fed to the feedback system for topographic scanning. The voltage signal from the current to voltage amplifier is also fed to the integrator of the potentiometry feedback circuit. The output of the integrator is then added with the non varying ac bias and supplied to one end of the sample. The output signal of the integrator added with the non varying ac bias is again added with a varying dc bias and the resultant is supplied from another end of the sample. This way, a constant ac bias is kept between the sample and the tip, but the dc bias can be varied to nullify the local potential between the tip and the sample. The dc voltage required to null the voltage between the tip and a point in the sample is actually the potential at that specific point. This dc voltage is then sent to the computer for imaging the potential distribution across the sample. For a material like LPCMO, the potential signal to be detected could be very small. The sensitivity of this detection depends on the bit size of the analog to digital converter (ADC) card. As you can see from the circuit diagram, two integrators are used in two feedback system. Care should taken not to use similar time constants for the two integrators. A separation of two time constants by a factor of 5-7 are reported [73] good enough to avoid the cross talk between the two integrators. This technique will be very useful to image a potential distribution of our LPCMO manganite which coexist in both metallic and insulating phase.

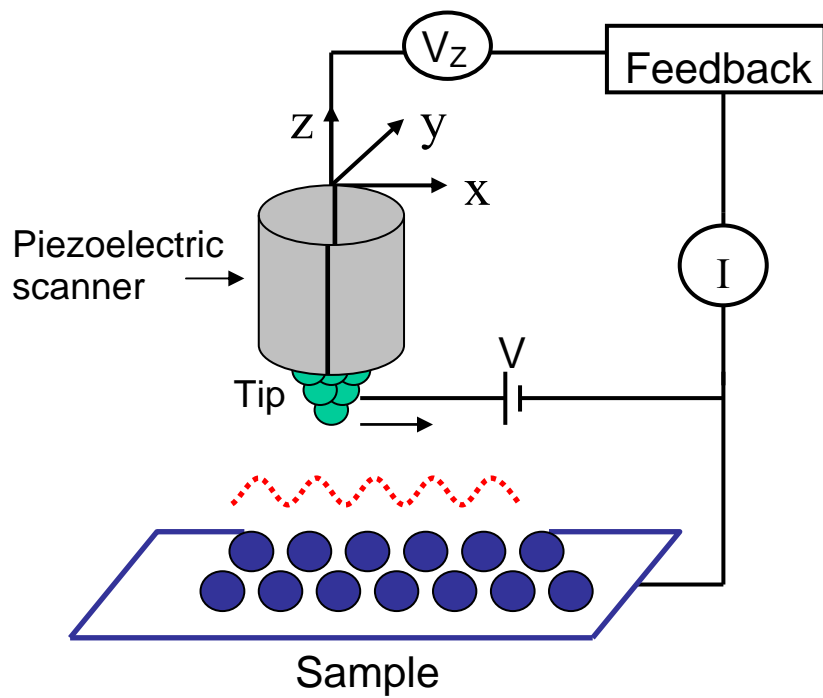


Figure 6-1: Schematic of scanning of STM tip in constant current mode. The dotted line gives the topography of one scan.

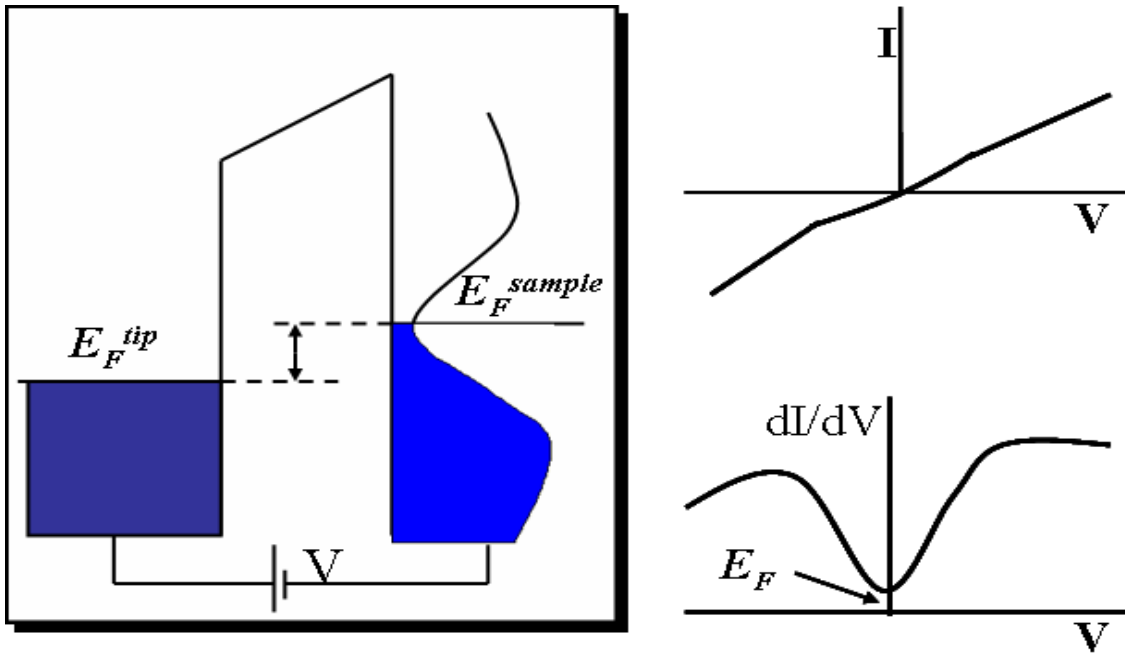


Figure 6-2: Schematic of the STM spectroscopic tunneling. The left side of the figure shows the relative Fermi levels when bias voltage V is applied. The wiggling vertical line on the sample side shows the different local density of states. When bias voltage is applied, the electron tunnels from the occupied states of the tip to the unoccupied states of the sample. The right side of the figure shows the computed spectroscopy characteristics.

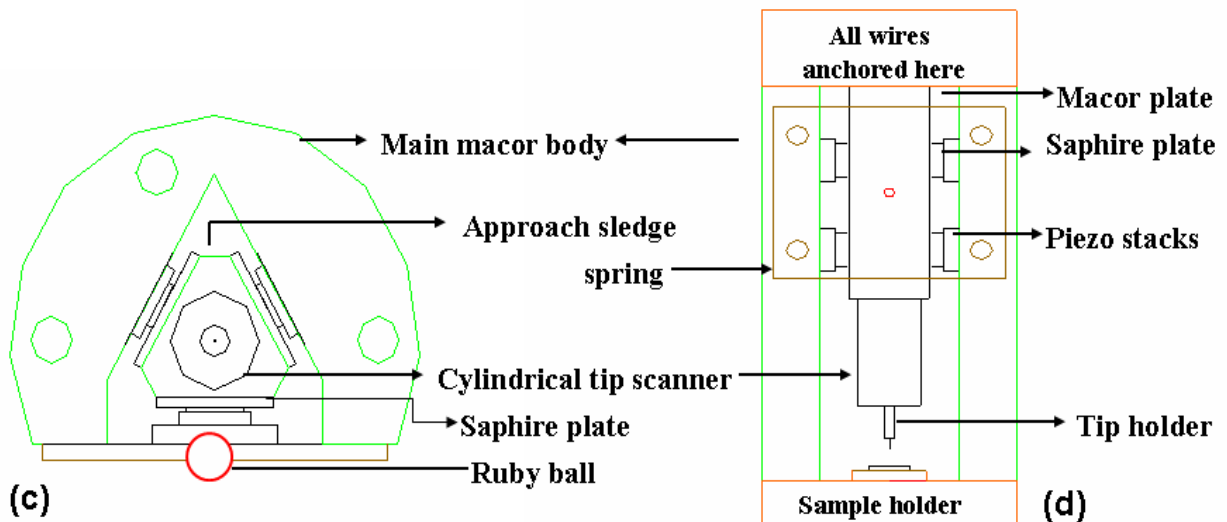
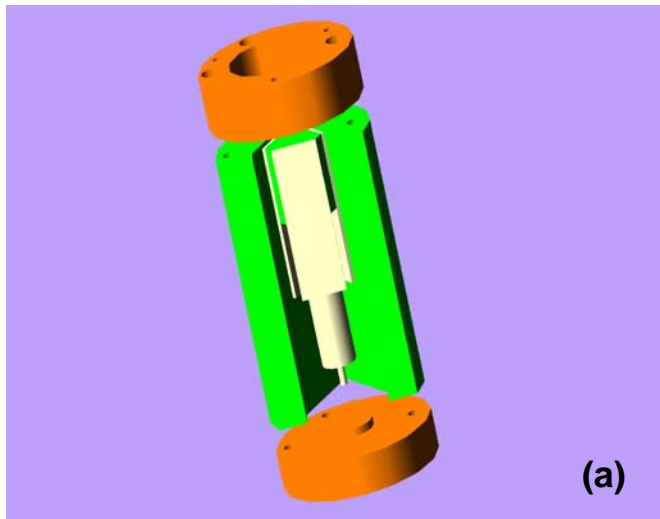


Figure 6-3: Design of different parts of the STM head. (a) 3-D AutoCAD drawing of the STM head. (b) Real picture of the STM head. (c) The top view drawing of the macor body with a V-shaped groove. (d) The front view of the macor cylinder. There are altogether 6 shear piezo stacks, 2 on each side of the macor cylinder and 2 beneath the macor plate. It holds the approach sledge with the ruby ball and spring plate on top of it. Sapphire plates are attached on top of the piezo stack. The spring plate made of phosphor bronze. All the wires from the STM head are anchored on the copper disk.

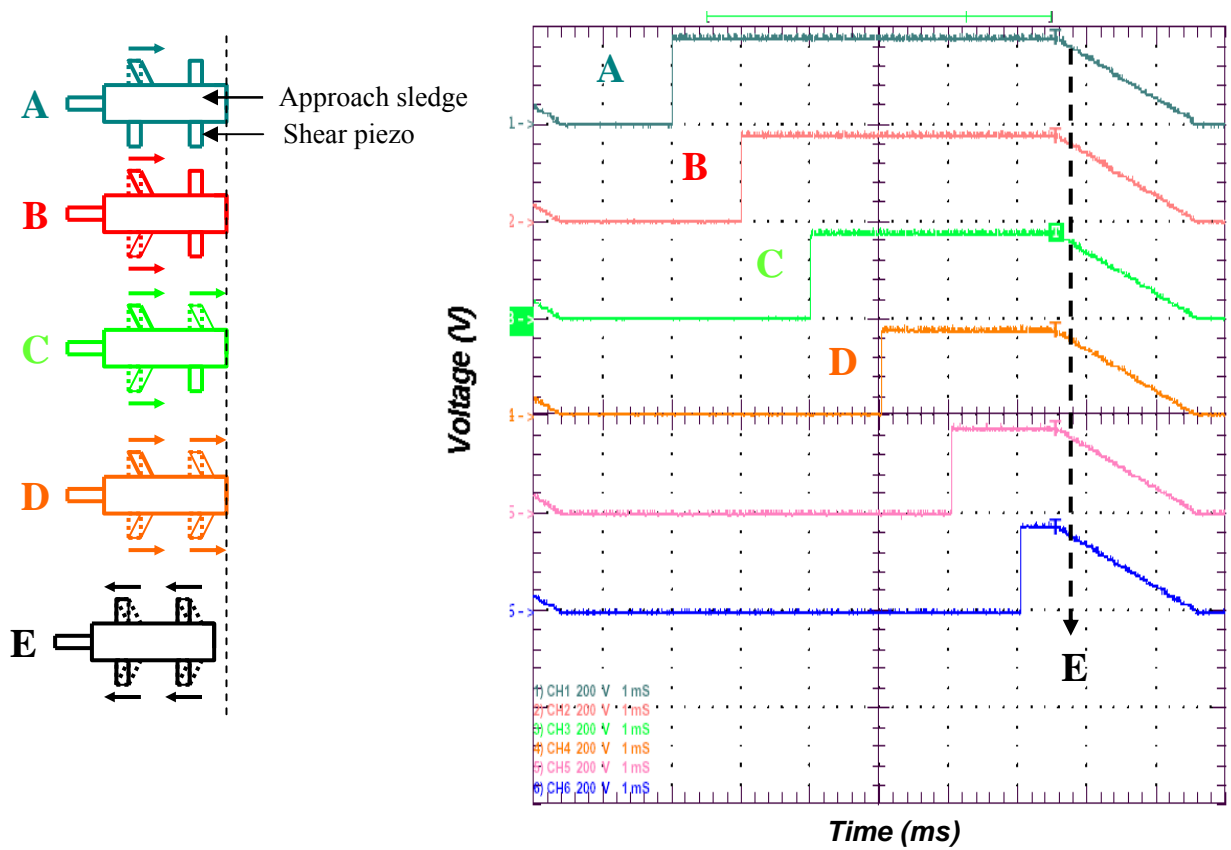


Figure 6-4: Voltage pulses in coarse approach mechanism (a) The top view of the triangular macor approach sledge held by shear piezo stacks on its sides. Two more shear piezo stacks on top are not shown. (b) High voltage amplifier positive output pulses to be applied at the shear piezo stacks for coarse approach.

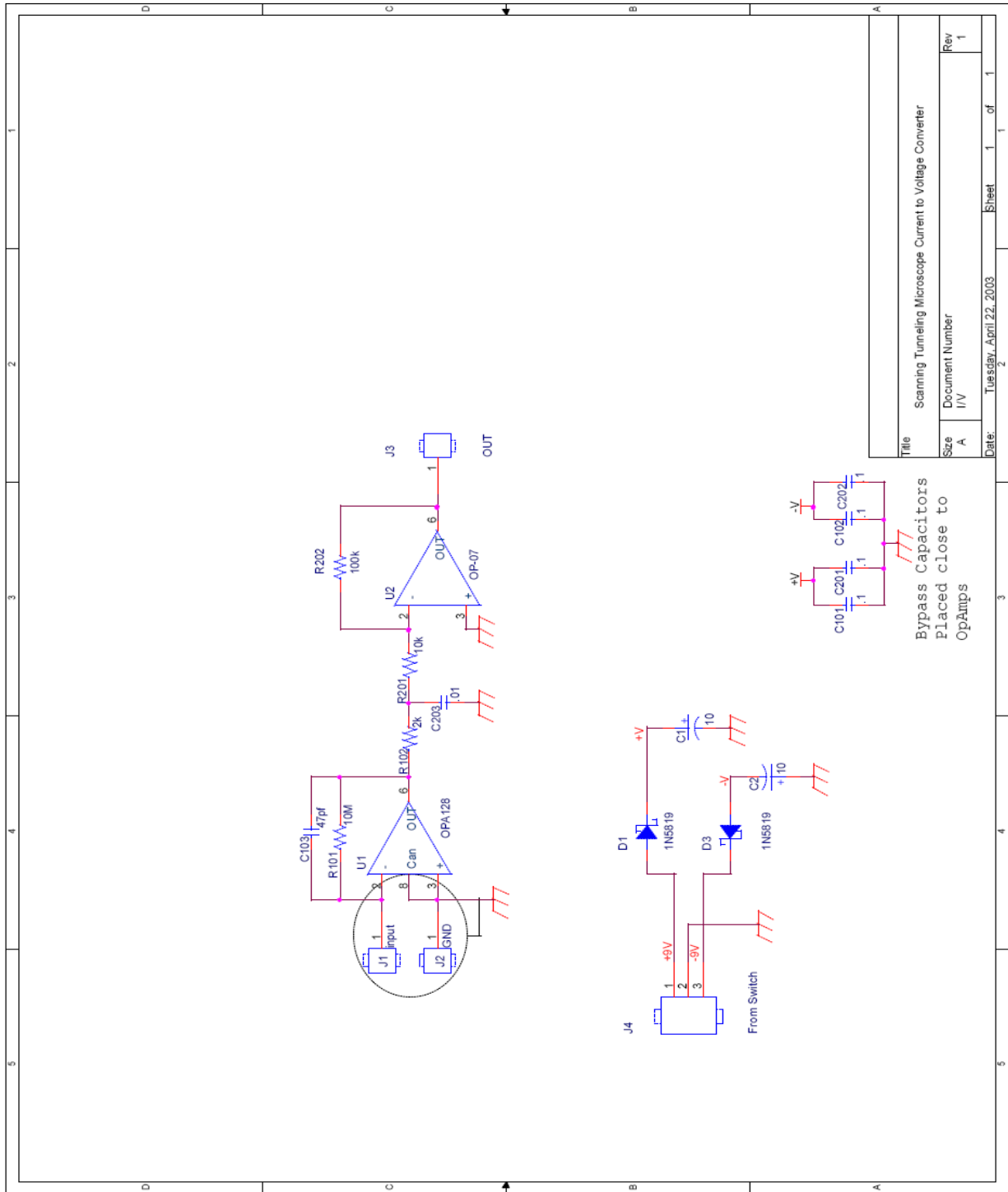


Figure 6-5: Current to voltage converter circuit for STM.

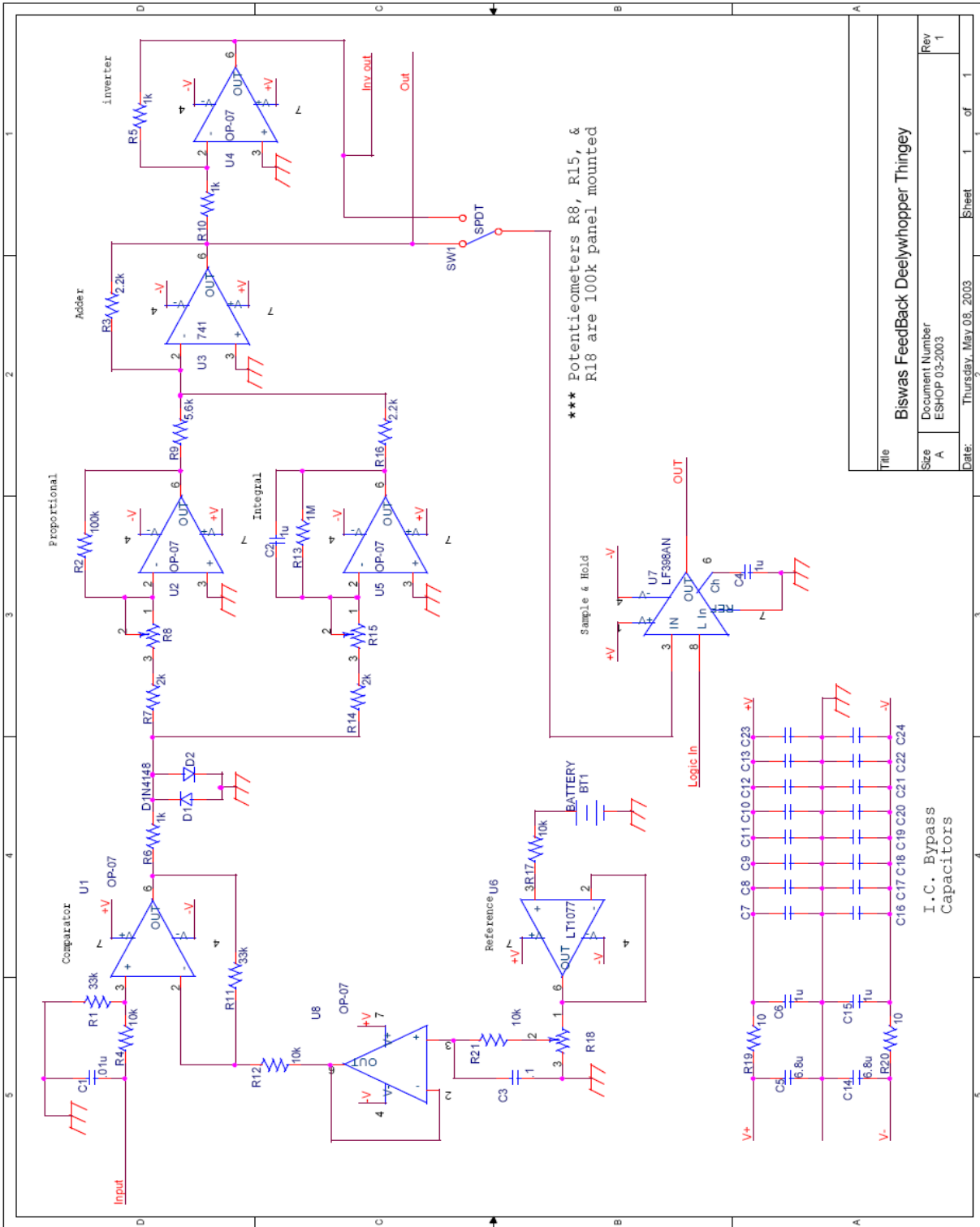


Figure 6-6: Feedback circuit for STM imaging. The proportional and Integral circuit are used.

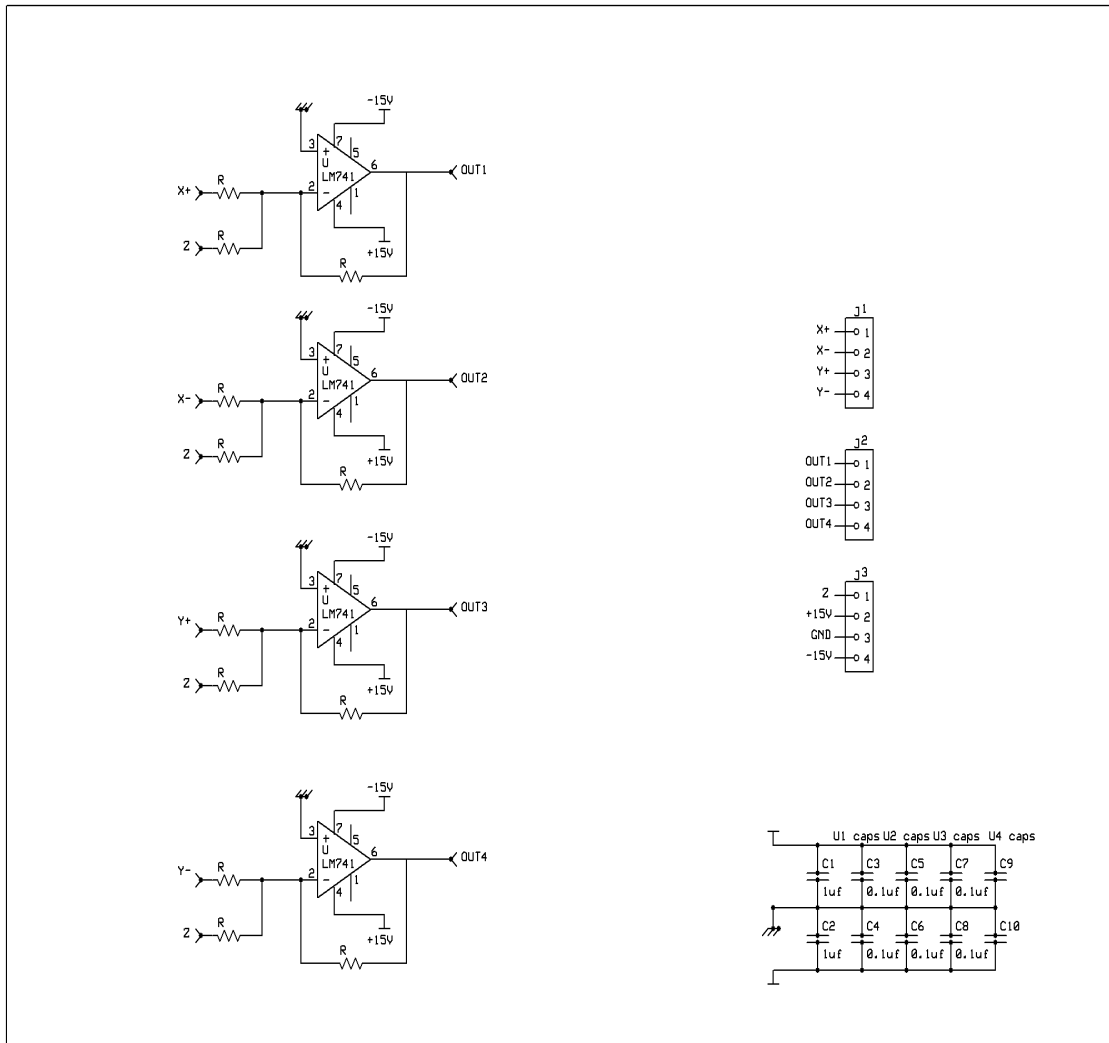


Figure 6-7: Summing circuit for the input of piezoelectric scanner.



Copper base



Copper cup

Figure 6-8: A vacuum can and a probe to hold the STM head. Left panel: A probe which holds the STM head on its copper base. Right panel: A vacuum can.



Figure 6-9: Vibration isolation system. The STM probe is put into the vibration isolation system once the tip and sample are in tunneling range. The sample transfer is done by a manipulator rod.

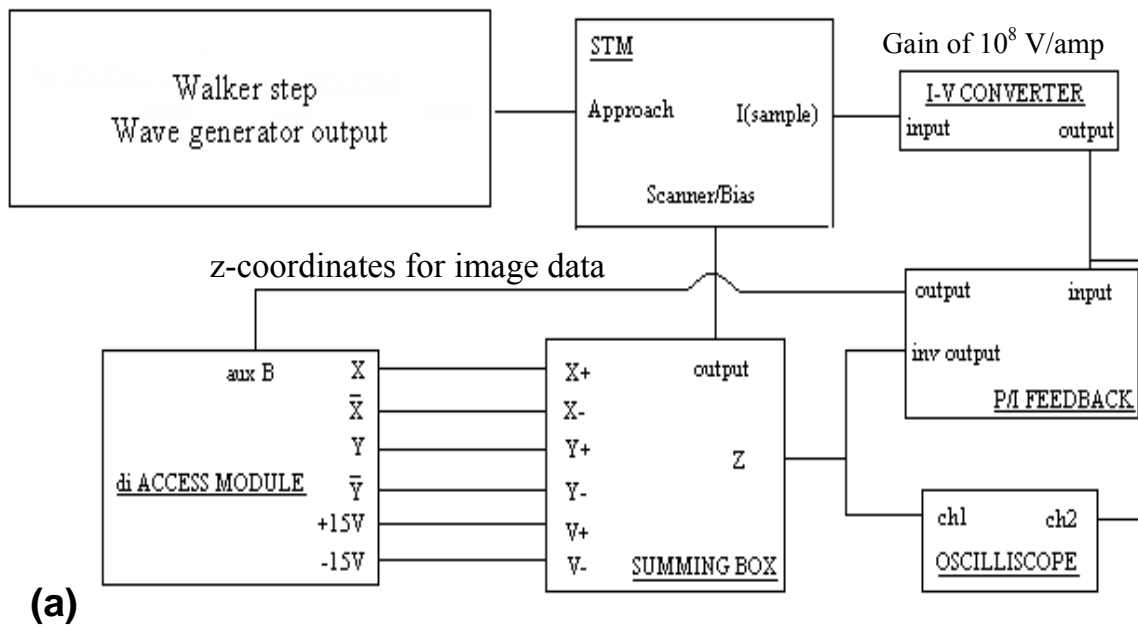


Figure 6-10: Scanning tunneling microscopy flow chart and electronics. (a) Flow chart for STM function. (b) Feedback circuit together with other electronics.

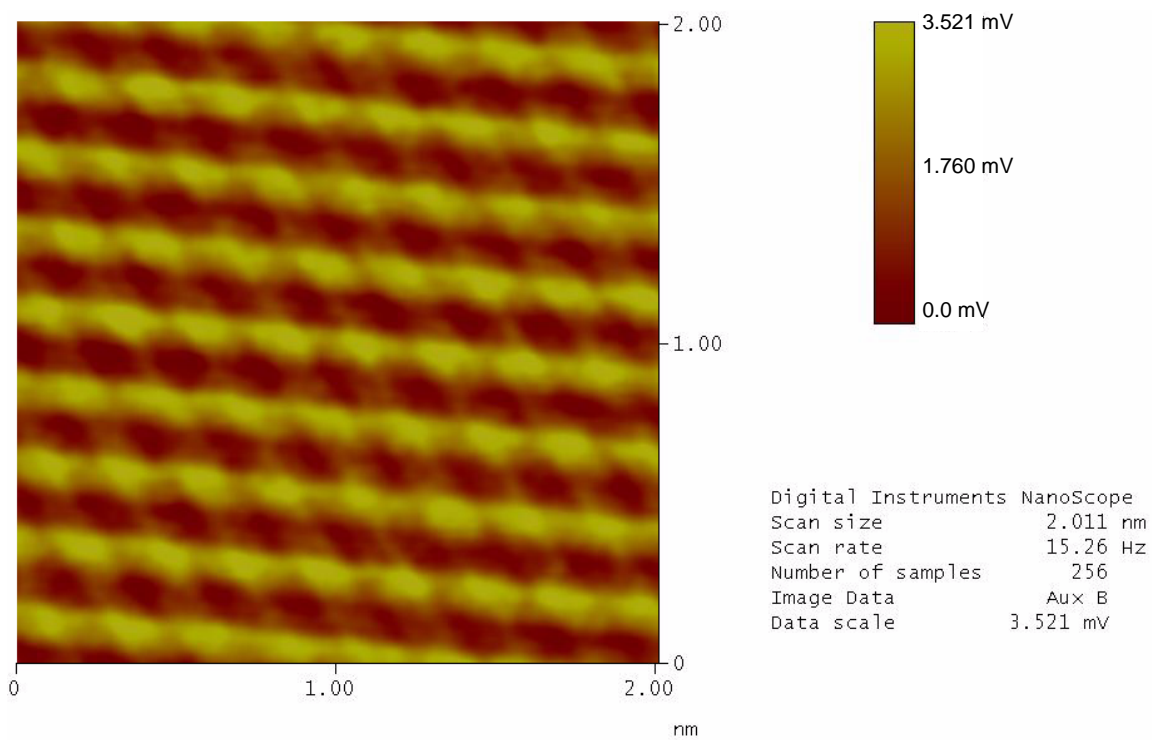


Figure 6-11: Calibration scan on graphite at room temperature

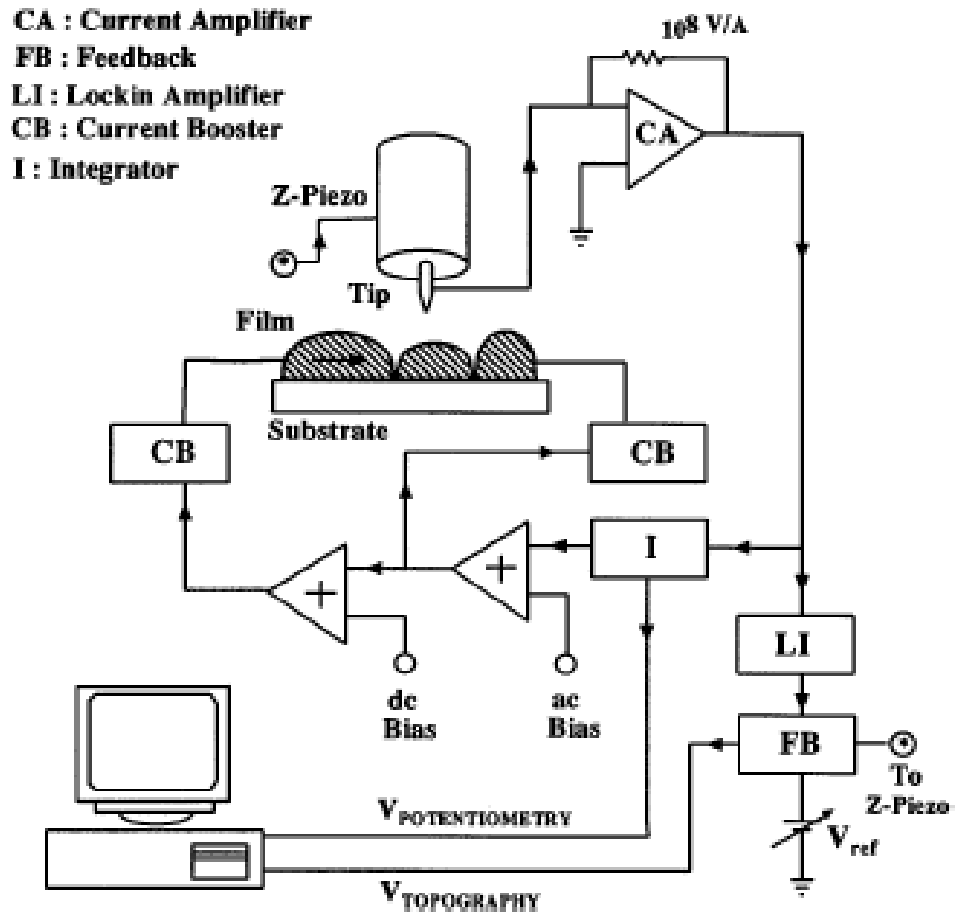


Figure 6-12: Scanning tunneling Potentiometry circuit diagram as taken from Ref. [73].

CHAPTER 7 CONCLUSION AND FUTURE WORK

Conclusion

We set up a pulsed laser deposition (PLD) lab for film growth. Thin films of phase separated manganites of the form $(La_{1-y}Pr_y)_{0.67}Ca_{0.33}MnO_3$ (where $y = 0.4, 0.5$ and 0.6) (LPCMO) were grown. The resistivity anomaly present at PMI-COI transition of the bulk LPCMO is removed in the thin film by substrate induced strain. In case of the LPCMO films grown on NGO (110) substrate, the low temperature strain stabilized the FMM phase. We created a phase diagram of LPCMO which clearly showed four distinct regions namely FMM, COI, FPS and SPS state. A strong electric field effect was observed when this material was in the FPS state. This electric field effect was used to manipulate the ferromagnetic domains in the FPS state by fabricating a nano-structure in the form of a cross bar. Our results showed that the FMM domains are stretched in the direction of the electric field applied but their overall volume remained same, which was confirmed by magnetization measurements. In addition, we built a low temperature STM which will be used to image the microscopic processes in phase separated manganites.

Future Work

Scanning Tunneling Potentiometry

To image a high resistance material like manganite using an STM is a difficult job since the sample and tunnel junction resistance may be comparable. But at low temperature, some of the manganites have low resistivity of about $1 \text{ m}\Omega\text{-cm}$ and can be considered as reasonably good metals. Some of these phase separated manganites we are working on have also shown the presence of thin insulating domain walls at low temperature when the bulk of the material is a good metal. This conclusion was drawn as tunneling magnetoresistance (TMR) effect was

observed by reducing the dimension of this material to nanometer scale [65]. To visually confirm the presence of the insulating domain walls, we will use our low temperature STM for scanning tunneling potentiometric [73, 74] images of manganite thin films.

Multiferroics

As explained throughout this dissertation, manganites show ferromagnetic properties. The ferromagnetic domains in manganites can be manipulated by using electric field. I would like to be involved in the search of the manganite based materials which show ferroelectricity [75] in addition to ferromagnetism. It has been observed in the compounds like RMnO_3 (R being Ho to Lu and Y) that magnetic and electric domains are coupled [76-79]. Since it is very rare to have a multiferroicity in one single material, I will also work in techniques to fabricate multiferroics in particular involving ferroelectric and ferromagnetic materials. I will use variable temperature magnetic force microscopy to see how the magnetic components are spread in the ferroelectric matrix. In addition I will also look for the possibility of fabricating devices incorporating manganites [80-83].

LIST OF REFERENCES

- [1] C.N.R. Rao and B. Raveau (Editors) *Colossal Magnetoresistance, charge ordering and Related Properties of Manganese Oxides*, World Scientific, Singapore (1998)
- [2] Y. Tokura, *Colossal Magnetoresistive Oxides*, Gordon and Breach Science Publishers, Singapore (2000)
- [3] M. B. Salamon and M. Jaime, *Review of Modern Physics* **73**, 583 (2001)
- [4] J. M. D. Coey, M. Viret, and S. von Molnar, *Adv. Phys.* **48**, 167 (1999)
- [5] L. Zhang, C. Israel, A. Biswas, R. L. Greene, and A. de Lozanne, *Science* **298**, 805 (2002)
- [6] M. Uehara, S. Mori, C. H. Chen, and S.-W. Cheong, *Nature* **399**, 560 (1999)
- [7] A. Asamitsu, Y. Tomioka, H. Kuwahara, and Y. Tokura, *Nature* **388**, 50 (1997)
- [8] V. Kiryukhin, Y. J. Wang, F. C. Chou, M. A. Kastner, and R. J. Birgeneau, *Phys. Rev. B* **59**, R6581 (1999)
- [9] A. Biswas, M Rajeswori, A.J. Millis and et al. *Phys. Rev. B* **63**, 184424 (2001)
- [10] Y. A. Soh, G. Aeppli, C. Y. Kim, N. D. Mathur, and M. G. Blamire, *J. Appl. Phys.* **93**, 8322 (2003)
- [11] G. Binasch, P. Grunberg, F. Saurenbach and W. Zinn, *Phys. Rev. B* **39**, 4828 (1989)
- [12] M. N. Baibich, J. M. Broto, A. Fert, F. Nguyen, V. Dau, F. Petroff, P. Eitenne, G. Creuzet, A. Friederich, and J. Chazelas, *Phys. Rev. Lett.* **61**, 2472 (1988)
- [13] S. Parkin, X. Jiang, C. Kaiser, A. Panchula, K. Roche, and M. Samant, *Proceedings of the IEEE*, **91**, 5 (2003)
- [14] C. Zener, *Phys. Rev.* **82**, 403 (1951)
- [15] C. Zener, *Phys. Rev.* **81**, 440 (1951)
- [16] P. W. Anderson and H. Hasegawa, *Phys. Rev.* **100**, 675 (1955)
- [17] G. H. Jonker and J. H. Van Santen, *Physica* **16**, 337 (1950); J. H. Van Santen and G.H. Jonker, *Physica* **16**, 599 (1950)
- [18] A.J. Millis, P.B. Littlewood and B. I. Shraiman, *Phys. Rev. Lett.* **74**, 5144 (1995)

- [19] C. Kittel, *Introduction to Solid State Physics*, 7th Edition., John Wiley & Sons, Inc., New York (2000)
- [20] N. W. Ashcroft and N. D. Mermin, *Solid State Physics*, Harcourt Asia Pte. Ltd., Singapore (2001)
- [21] S. Mercone, C. A. Perroni, V. Cataudella, C. Adamo, M. Angeloni, C. Aruta, G. De Filippis, F. Miletto, A. Oropallo, P. Perna, A. Yu. Petrov, U. Scotti di Uccio, and L. Maritato, *Phys. Rev. B* **71**, 064415 (2005)
- [22] P. Schiffer, A.P. Ramirez, W. Bao. S.W. Cheong, *Phys. Rev. Lett.* **75**, 3336 (1995)
- [23] H.A. Jahn and E. Teller, *Proc. Roy. Soc. A* **161**, 220 (1937)
- [24] A.J. Millis, *Nature* **392**, 147 (1998)
- [25] S. Satpathy *et al*, *J. Appl. Phys.* **79**, 4555 (1996)
- [26] I. Solovyev, N. Hamada, and K. Terakura, *Phys. Rev. Lett*, **76**, 4825 (1996)
- [27] Y. Tokura and N. Nagaosa, *Science* **288**, 462 (2000)
- [28] T. Mizokawa and A. Fujimori, *Phys. Rev. B* **54**, 5368 (1996)
- [29] S. Ishihara, J. Inoue, S. Maekawa, *Phys. Rev. B* **55**, 8280 (1997)
- [30] Y. Tomioka, A Asamitsu et al. *Physica B* **6**, 237 (1997)
- [31] Y. Tomioka, A Asamitsu et al. *Phys. Rev. Lett.* **74**, 5108 (1995)
- [32] S. Mori, C. H. Chen and S.W. Cheong, *Nature* **392**, 473 (1998)
- [33] J.C. Loudon, N.D. Mathur, P.A. Midgley, *Journal of Magnetism and Magnetic Materials* **272–276**, 13 (2004)
- [34] N. Mathur and P. Littlewood. *Physics Today* **56**, 25 (2003)
- [35] H. A. Jahn and E. Teller , *Proceedings of the Royal Society of London. Series A, Mathematical and Physical Science*, **161** (905), 220-235 (1937)
- [36] A. Biswas, M. Rajeswari, R. C. Srivastava, Y. H. Li, T. Venkatesan, R. L. Greene, and A. J. Millis, *Phys. Rev. B* **61**, 9665 (2000)
- [37] C. W. Yuan, E. Batalla, A. de Lozanne, M. Kirk, and M. Tortonese, *Appl. Phys. Lett.* **65**, 1308 (1994)

- [38] C. W. Yuan, Z. Zheng, A. L. de Lozanne, M. Tortonese, D. A. Rudman, and J. N. Eckstein, *J. Vac. Sci. Technol. B* **14**, 1210 (1996)
- [39] Y Tomioka, A. Asamitsu and *et al.* *Phys Rev B* **53**, R1689 (1996)
- [40] D. B. Chrisey, G. K. Hubler *Pulsed Laser Deposition of Thin Films*, Wiley-VCH, New York (2003)
- [41] G. Binnig, C. F. Quate, and Ch. Gerber, *Phys. Rev. Lett.* **56**, 930 (1986)
- [42] J. K. H. Horber and M. J. Miles, *Science* **302**, 1002 (2003)
- [43] F. Oesterhelt, D. Oesterhelt, M. Pfeiffer, A. Engel, H. E. Gaub, and D. J. Muller, *Science* **288**, 143 (2000)
- [44] K. H. Ahn, T. Lookman, and A. R. Bishop, *Nature* **428**, 401 (2004)
- [45] E. Dagotto, *Science* **309**, 257 (2005)
- [46] H. Y. Hwang, S.-W. Cheong, P. G. Radaelli, M. Marezio, and B. Batlogg, *Phys. Rev. Lett.* **75**, 914 (1995)
- [47] V. Podzorov, B. G. Kim, V. Kiryukhin, M. E. Gershenson, and S-W. Cheong, *Phys. Rev. B* **64**, 140406(R) (2001)
- [48] G. C. Milward, M. J. Calderón, and P. B. Littlewood, *Nature* **433**, 607 (2005)
- [49] P. G. de Gennes, *The Physics of Liquid Crystals*, Oxford University Press, New York (1995).
- [50] C. Aruta, G. Ghiringhelli, A. Tebano, N. G. Boggio, N. B. Brookes, P. G. Medaglia, and G. Balestrino, *Phys. Rev. B* **73**, 235121 (2006)
- [51] Y. L. Li, S. Y. Hu, Z. K. Liu, and L. Q. Chen, *Acta Mater.* **50**, 395 (2002)
- [52] P. A. Sharma, S. B. Kim, T. Y. Koo, S. Guha, and S-W. Cheong, *Phys. Rev. B* **71**, 224416 (2005); L. Ghivelder and F. Parisi, *ibid.* **71**, 184425 (2005)
- [53] D. E. Cox, P. G. Radaelli, M. Marezio, and S-W. Cheong, *Phys. Rev. B* **57**, 3305 (1998)
- [54] W. Prellier, A. Biswas, M. Rajeswari, T. Venkatesan, and R. L. Greene, *Appl. Phys. Lett.* **75**, 397 (1999)
- [55] W. Pompe, X. Gong, Z. Suo, and J. S. Speck, *J. Appl. Phys.* **74**, 6012 (1993)

- [56] N. K. Pandey, R. P. S. M. Lobo, and R. C. Budhani, Phys. Rev. B **67**, 054413 (2003)
- [57] M. Tokunaga, Y. Tokunaga, and T. Tamegai, Phys. Rev. Lett. **93**, 037203 (2004); M. Tokunaga, H. Song, Y. Tokunaga, and T. Tamegai, *ibid.* **94**, 157203 (2005)
- [58] R. Y. Gu, Z. D. Wang, and C. S. Ting, Phys. Rev. B **67**, 153101 (2003)
- [59] T. Dhakal, J. Tosado, A. Biswas, Phys. Rev. B **75**, 092404 (2007)
- [60] D. J. Griffiths, *Introduction to Electrodynamics*, Third Edition, Prentice-Hall, Inc., Englewood Cliffs, NJ (1999)
- [61] M. Matsukawa, K. Akasaka, H. Noto, R. Suryanarayanan, S. Nimori, M. Apostu, Phys. Rev. B **72**, 064412 (2005)
- [62] P. D. Beale and P.M. Duxbury, Phys Rev B **37**, 2785 (1998)
- [63] G. Garbarino, C. Acha, P. Levy, T. Y. Koo, and S-W. Cheong, Phys. Rev. B **74**, 100401(R) (2006)
- [64] T. Wu and J. F. Mitchell, Phys. Rev. B **74**, 214423 (2006)
- [65] G. Singh-Bhalla, S. Selcuk, T. Dhakal, A. Biswas, A. F. Hebard, arXiv:0707.4411(2007)
- [66] Ch. Renner, G. Aeppli, B.-G. Kim, Yeong-Ah Soh and S.-W. Cheong, Nature **416**, 518 (2002)
- [67] M. Fäth, S. Freisem, A. A. Menovsky, Y. Tomioka, J. Aarts and J. A. Mydosh, Science **285**, 1540 (1999)
- [68] G. Binnig, H. Rohrer, Ch. Gerber, and E. Weibel, Phys. Rev. Lett., **49**, 57 (1982)
- [69] G. Binnig, H. Rohrer, Ch. Gerber, and E. Weibel, Appl. Phys. Lett., **40**, 178 (1982)
- [70] G. Binnig, H. Rohrer, Ch. Gerber, and E. Weibel, Phys. Rev. Lett., **50**, 120 (1983)
- [71] R. Wiesendanger, *Scanning Probe Microscopy and Spectroscopy, Methods and Applications*, Cambridge University Press, Cambridge (1998)
- [72] S. H. Pan, E. W. Hudson, and J. C. Davis, Review of Scientific Instruments **70**, 1459 (1999)
- [73] G. Ramaswamy, A.K. Raychaudhuri, K. Das Gupta, G. Sambandamurthy. Applied Physics A, **66**, S435 (1998)

- [74] P. Muralt and D.W. Pohl, Appl. Phys. Lett **48**, 514 (1986)
- [75] T. Goto, T. Kimura, G. Lawes, A. P. Ramirez, and Y. Tokura, Phys. Rev. Lett. **92**, 257201 (2004)
- [76] M. Fiebig, Th. Lottermoser, D. Frohlich, A.V. Goltsev and R.V. Pisarev, Nature **419**, 818 (2002)
- [77] B. B. Van Aken, T. T. M. Palstra, A. Filippetti, and N. A. Spaldin, Nature Materials **3**, 164 (2004)
- [78] R. Vasic, H. D. Zhou, E. Jobiliong, C. R. Wiebe, and J. S. Brooks, Phys. Rev. B **75**, 014436 (2007)
- [79] V. Laukhin, V. Skumryev, X. Martí, D. Hrabovsky, F. Sánchez, M. V. García-Cuenca, C. Ferrater, M. Varela, U. Lüders, J. F. Bobo, and J. Fontcuberta, Phys. Rev. Lett. **97**, 227201 (2006)
- [80] R. P. Rairigh, G. Singh-Bhalla, S. Tongay, T. Dhakal, A. Biswas, A. F. Hebard, Nature Physics **3**, 551(2007)
- [81] T. Wu, S. B. Ogale, J. E. Garrison, B. Nagaraj, Amlan Biswas, Z. Chen, R. L. Greene, R. Ramesh, T. Venkatesan, and A. J. Millis, Phys. Rev. Lett. **86**, 5998 (2001)
- [82] Y. Hikita, Y. Kozuka, T. Susaki, H. Takagi, and H. Y. Hwang, Appl. Phys. Lett. **90**, 143507 (2007)
- [83] Y. Ogimoto, M. Izumi, A. Sawa, T. Manako, H. Sato, H. Akoh, M. Kawasaki, and Y. Tokura. Jpn. J. Appl. Phys., Part 2 **42**, L369 (2003)

BIOGRAPHICAL SKETCH

Tara Dhakal was a fourth child of his parents and was born in a small village called Punarbas, in the far western part of Nepal. After graduating from Punarbas Janata High School, he went to the beautiful tourist city of Pokhara, where he joined Prithvi Narayan College affiliated under Tribhuvan University for his undergraduate degree in physics, mathematics, and statistics. He finished his undergraduate degree as valedictorian in 1994. For this he was awarded a gold medal from King Birendra of Nepal. In 1995 he joined the central department of physics, Tribhuvan University, Kathmandu, Nepal, for his master's degree in physics. He went to Japan in 1998 to pursue an M.S. in material science from Shimane University under a Japanese government scholarship (Monbusho). There, he studied the effect of doping on the transport properties of hole-doped manganites. He also prepared and studied samples of high T_c superconductors. He graduated from the material science department, Shimane University, Matsue, Japan, with an M.S. degree in physics in May 2001.

He then joined the University of Florida in summer 2002. During that summer he worked in Prof. Hills's lab to study organic superconductor by using micro waves. In 2003 he joined the Biswas lab for his PhD research. He started to study the properties of phase separated manganite by using bulk probes like magneto-transport and local probes like the low temperature scanning tunneling microscope (LTSTM). He was able to find a region of this material where it acts like an electronic soft matter where the magnetic domains can be manipulated by using electric field. He also helped to set up a new lab and built a low temperature scanning tunneling microscope (LTSTM). He is planning to use his recently built LTSTM to image the phase coexistence in manganites by using a technique called scanning tunneling potentiometry (STP). In the future, he plans to study multiferroics by using tools like the low temperature scanning tunneling microscopy, the low temperature magnetic force microscopy, and transport measurements.